Fast, sensitive and accurate integration of single-cell data with Harmony

Ilya Korsunsky [1,2,3,4], Nghia Millard[1,2,3,4], Jean Fan [5], Kamil Slowikowski[1,2,3,4], Fan Zhang [1,2,3,4], Kevin Wei[2], Yuriy Baglaenko [1,2,3,4], Michael Brenner[2], Po-ru Loh [1,3,4] and Soumya Raychaudhuri [1,2,3,4,6]*

The emerging diversity of single-cell RNA-seq datasets allows for the full transcriptional characterization of cell types across a wide variety of biological and clinical conditions. However, it is challenging to analyze them together, particularly when datasets are assayed with different technologies, because biological and technical differences are interspersed. We present Harmony (https://github.com/immunogenomics/harmony), an algorithm that projects cells into a shared embedding in which cells group by cell type rather than dataset-specific conditions. Harmony simultaneously accounts for multiple experimental and biological factors. In six analyses, we demonstrate the superior performance of Harmony to previously published algorithms while requiring fewer computational resources. Harmony enables the integration of ~10^6 cells on a personal computer. We apply Harmony to peripheral blood mononuclear cells from datasets with large experimental differences, five studies of pancreatic islet cells, mouse embryogenesis datasets and the integration of scRNA-seq with spatial transcriptomics data.

Recent technological advances[1] enable unbiased single-cell transcriptional profiling of thousands of cells in one experiment. Projects such as the Human Cell Atlas[2] (HCA) and Accelerating Medicines Partnership[3–5] exemplify the growing body of reference datasets of primary human tissues. While individual experiments incrementally expand our understanding of cell types, a comprehensive catalog of healthy and diseased cells will require the ability to integrate multiple datasets across donors, studies and technological platforms. Moreover, in translational research, joint analyses across tissues and clinical conditions will be essential to identify disease-expanded populations. Since meaningful biological variation in single-cell RNAseq datasets from different studies is often confounded by data source[6], investigators have developed unsupervised multi-dataset integration algorithms[7–10]. These methods embed cells from diverse experimental conditions and biological contexts into a common reduced dimensional embedding to enable shared cell-type identification across datasets.

Here, we introduce Harmony, an algorithm for robust, scalable and flexible multi-dataset integration to meet four key challenges of unsupervised scRNAseq joint embedding: scaling to large datasets, identification of both broad populations and fine-grained subpopulations, flexibility to accommodate complex experimental design, and the power to integrate across modalities. We apply Harmony to a diverse range of examples, including cell lines, peripheral blood mononuclear cells (PBMCs) assayed with different technologies, a meta-analysis of pancreatic islet cells from multiple donors and studies, longitudinal samples from mouse embryogenesis, and cross-modality integration of scRNA-seq data with spatial transcriptomics data. Harmony is available as an R package on github (https://github.com/immunogenomics/harmony), with functions for standalone and Seurat[7] pipeline analyses.

Results

Harmony iteratively learns a cell-specific linear correction function. Harmony begins with a low-dimensional embedding of cells, such as principal components analysis (PCA), (Supplementary Note 1 and Methods). Using this embedding, Harmony first groups cells into multi-dataset clusters (Fig. 1a). We use soft clustering to assign cells to potentially multiple clusters, to account for smooth transitions between cell states. These clusters serve as surrogate variables, rather than to identify discrete cell types. We developed a new soft k-means clustering algorithm that favors clusters with cells from multiple datasets (Methods). Clusters disproportionately containing cells from a small subset of datasets are penalized by an information theoretic metric. Harmony allows for multiple different penalties to accommodate multiple technical or biological factors, such as different batches and tissue sources. Soft clustering preserves discrete and continuous topologies while avoiding local minima that might result from maximizing representation too quickly across multiple datasets. After clustering, each dataset has cluster-specific centroids (Fig. 1b) that are used to compute cluster-specific linear correction factors (Fig. 1c). Since clusters correspond to cell types and states, cluster-specific correction factors correspond to individual cell-type and cell-state specific correction factors. In this way, Harmony learns a simple linear adjustment function that is sensitive to intrinsic cellular phenotypes. Finally, each cell is assigned a cluster-weighted average of these terms and corrected by its cell-specific linear factor (Fig. 1d). Since each cell may be in multiple clusters, each cell has a potentially unique correction factor. Harmony iterates these four steps until cell cluster assignments are stable.

Quantifying performance in cell-line data. We first assessed Harmony using three carefully controlled datasets, to evaluate
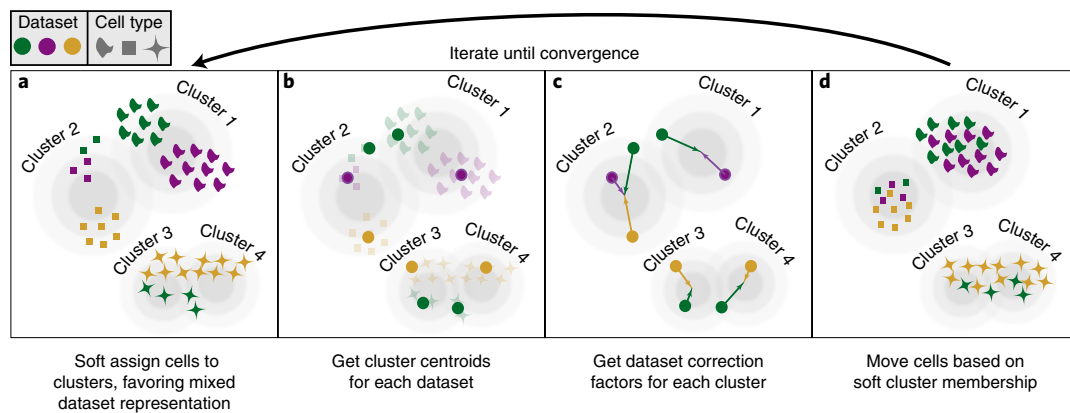
Fig. 1 | Overview of Harmony algorithm. PCA embeds cells into a space with reduced dimensionality. Harmony accepts the cell coordinates in this reduced space and runs an iterative algorithm to adjust for dataset specific effects. **a**, Harmony uses fuzzy clustering to assign each cell to multiple clusters, while a penalty term ensures that the diversity of datasets within each cluster is maximized. **b**, Harmony calculates a global centroid for each cluster, as well as dataset-specific centroids for each cluster. **c**, Within each cluster, Harmony calculates a correction factor for each dataset based on the centroids. **d**, Finally, Harmony corrects each cell with a cell-specific factor: a linear combination of dataset correction factors weighted by the cell's soft cluster assignments made in step **a**. Harmony repeats steps **a** to **d** until convergence. The dependence between cluster assignment and dataset diminishes with each round. Datasets are represented with colors, cell types with different shapes.

performance on both integration (mixing of datasets) and accuracy (no mixing of cell types). Perfect integration can be achieved by mixing all cells, regardless of cellular identity. Similarly, high accuracy can be achieved by partitioning cells into broad clusters without mixing datasets in small neighborhoods. In this situation, broad cellular states are defined, but fine-grained cellular substates and subtypes are confounded by the originating dataset. To quantify integration and accuracy of this embedding, we defined an objective metric: the local inverse Simpson's Index (LISI, see Methods) in the local neighborhood of each cell. To assess integration, we employ 'integration LISI' (iLISI, see Fig. 2a), which defines the effective number of datasets in a neighborhood. Neighborhoods represented by only a single dataset get an iLISI of 1, while neighborhoods with an equal number of cells from two datasets get an iLISI of 2. Note that even under ideal mixing, if the datasets have different numbers of cells, iLISI would be less than 2. To assess accuracy, we use 'cell-type LISI' (cLISI, see Fig. 2b), the same mathematical measure, but applied to cell type instead of dataset labels. Accurate integration should maintain a cLISI of 1, reflecting a separation of unique cell types throughout the embedding. An erroneous embedding would include neighborhoods with a cLISI of 2, indicating that neighbors have two different types of cell.

We begin with three datasets from two cell lines: (1) pure Jurkat, (2) pure 293T and (3) a 50/50 mix[11]. These datasets are ideal for illustration and for assessment, as each cell can be unambiguously labeled Jurkat or 293T (Supplementary Fig. 1a). A thorough integration would mix the 1,799 Jurkat cells from the mixture dataset with 3,255 cells from the pure Jurkat dataset and the 1,565 293T cells from the mixture dataset with the 2,859 from the pure 293T dataset. Thus, we expect the average iLISI to range from 1, reflecting no integration, to 1.8 $(=1/[(1{,}799/(1{,}799+2{,}859))^2+(3{,}255/(1{,}799+3{,}255))^2])$ for Jurkat cells and 1.5 $(=1/[(1{,}565/(1{,}565+2{,}859))^2+(2{,}859/(1{,}565+2{,}859))^2])$ for 293T cells, reflecting maximal accurate integration. Application of a standard PCA pipeline followed by UMAP embedding demonstrates that the cells group broadly by dataset and cell type. This is both visually apparent and quantified (Fig. 2c,d) with high accuracy reflected by a low cLISI (median iLISI 1.00, 95% confidence interval (CI) [1.00, 1.00]). However, the iLISI (median iLISI 1.01, 95% CI [1.00, 1.61]) is also low, reflecting imperfect integration and ample structure within each cell type reflecting the dataset of origin. After

Harmony, cells from the 50/50 dataset are appropriately mixed into the pure datasets (Fig. 2e). The increased iLISI (median iLISI 1.59, 95% CI [1.27, 1.97]) reflects the mixing of datasets, while the low cLISI (Fig. 2f, median iLISI 1.00, 95% CI [1.00, 1.02]) reflects the accurate separation of Jurkat from 293T cells. iLISI and cLISI provide a quantitative way to compare the integration and accuracy of multiple algorithms. We repeated the integration and LISI analyses with MNN Correct, BBKNN, MultiCCA and Scanorama and showed that they produced embeddings with statistically inferior integration (Supplementary Results, Fig. 1b and Table 1).

This benchmark demonstrates the two key metrics for assessing mixing and accuracy and shows that Harmony performs well on both metrics in a well-controlled analysis of cell-line datasets. A potential pitfall of LISI is that it is sensitive to datasets of vastly different sizes. In such a situation, most neighborhoods can be dominated by a single dataset and LISI values become difficult to interpret (Supplementary Note 2).

Harmony scales to large data. We evaluated Harmony's computational performance, measuring both total runtime and maximum memory usage. To demonstrate Harmony's scalability versus other methods, we downsampled HCA data[12] (528,688 cells from 16 donors and two tissues) to create five benchmark datasets with 500,000, 250,000, 125,000, 60,000 and 30,000 cells. We reported the runtime and memory (Supplementary Tables 2 and 3) for all benchmarks. Harmony runtime scaled well for all datasets (Fig. 3a), ranging from 4 min on 30,000 cells to 68 min on 500,000 cells, 30 to 200 times faster than MultiCCA and MNN Correct. The runtimes for Harmony, BBKNN and Scanorama were comparable for datasets with up to 125,000 cells. Harmony required dramatically less memory (Fig. 3b) compared to other algorithms: only 0.9 gigabytes (GB) on 30,000 cells and 7.2 GB on 500,000 cells. At 125,000 cells, Harmony required 30–50 times less memory than Scanorama, MNN Correct and Seurat MultiCCA; these other methods could not scale beyond 125,000 cells. Harmony returned substantially more integrated embeddings (Fig. 3c) than did other competing algorithms (Supplementary Results), allowing for the identification of shared cell types (Fig. 3d) across tissues and donors. These results demonstrate that Harmony is computationally efficient and capable of analyzing even large datasets (10^5–10^6 cells) on personal computers.
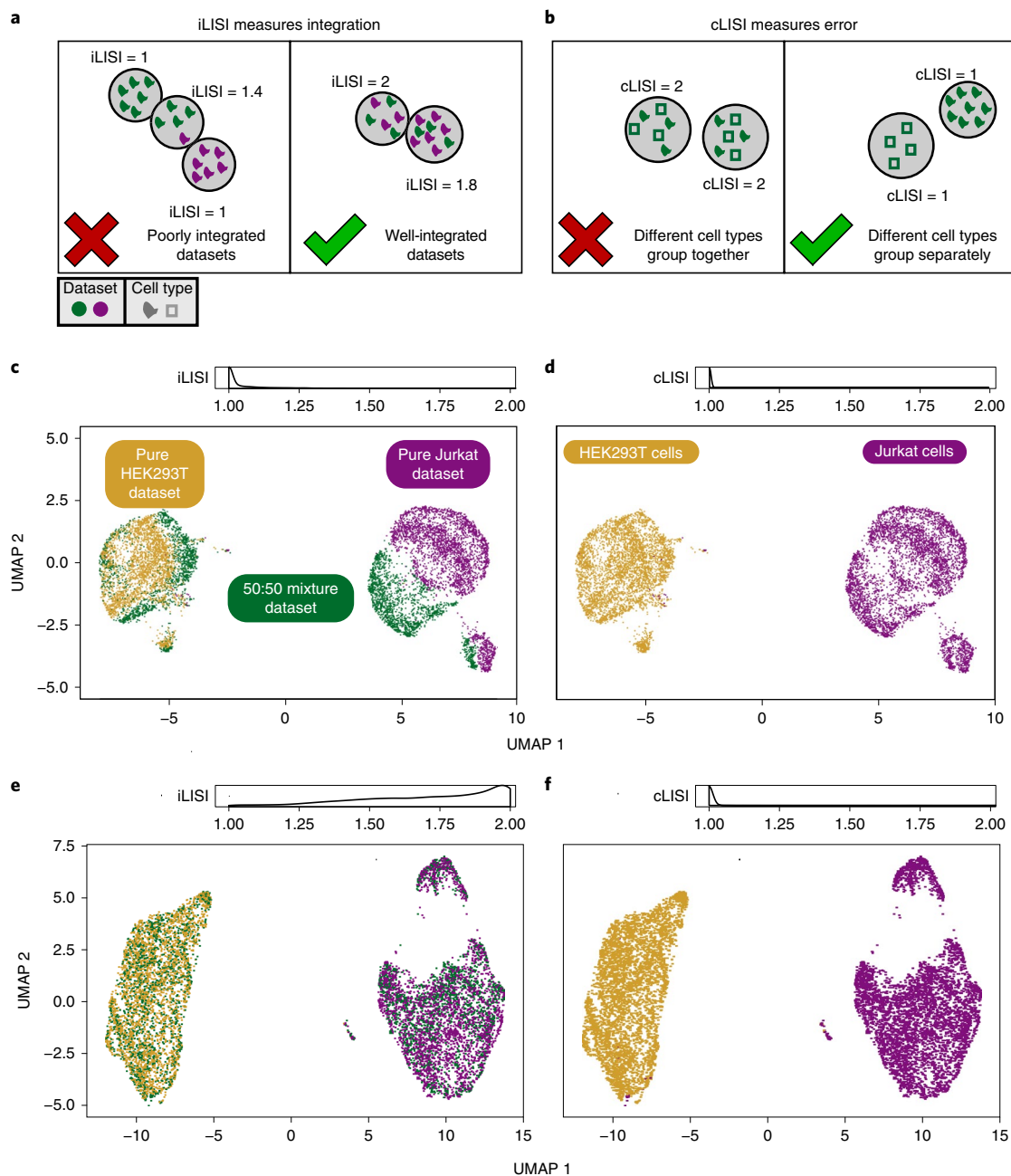
Fig. 2 | Quantitative assessment of dataset mixing and cell-type accuracy with cell-line datasets. a, iLISI measures the degree of mixing among datasets in an embedding, ranging from 1 in an unmixed space to *B,* the number of datasets in the analysis, in a well mixed space. **b**, cLISI measures integration accuracy using the same formulation but computed on cell-type labels instead. An accurate embedding has a cLISI close to 1 for every neighborhood, reflecting separation of different cell types. $n = 3,255$ Jurkat and $n = 2,859$ human embryonic kidney 293T (HEK293T) cells from pure (purple and yellow) cell-line datasets and $n = 1,799$ Jurkat and $n = 1,565$ HEK293T cells from a mixed (green) cell-line dataset were analyzed together. **c,d**, Before Harmony integration, cells grouped by dataset (**c**) and known cell type (**d**). iLISI (**c**) and cLISI (**d**) were computed for every cell's neighborhood and summarized with density plots. **e,f**, After Harmony integration, cells from the mixture dataset are mixed into the other datasets (**e**), achieved by mixing Jurkat with Jurkat cells and HEK293T with HEK293T cells (**f**). iLISI (**e**) and cLISI (**f**) were re-computed in the Harmony embedding.

Identification of broad and fine-grained PBMC subpopulations.
To assess how Harmony might perform under more challenging scenarios, we gathered three datasets of human PBMCs, each assayed on the Chromium 10X platform but prepared with different protocols: 3′ end v1 (3pV1), 3′ end v2 (3pV2) and 5′ end (5p) chemistries. After pooling all the cells together, we performed a joint analysis. Before integration, cells group primarily by dataset (Fig. 4a, median iLISI 1.00, 95% CI [1.00, 1.00]).

Harmony clustered the cells into biologically coherent groups (Supplementary Fig. 6a) and removed dataset-specific variation within each cluster. In the final integrated space, the datasets are well mixed (Fig. 4b, median iLISI 1.96, 95% CI [1.36, 2.56]), more so than with other methods (median iLISI 1.02, 95% CI [1.00, 2.11]). We confirmed that >83% of cells had a significantly (false discovery rate (FDR) < 5%) higher iLISI value in Harmony than with any other algorithm (Supplementary Fig. 6b,c). To assess accuracy, within each
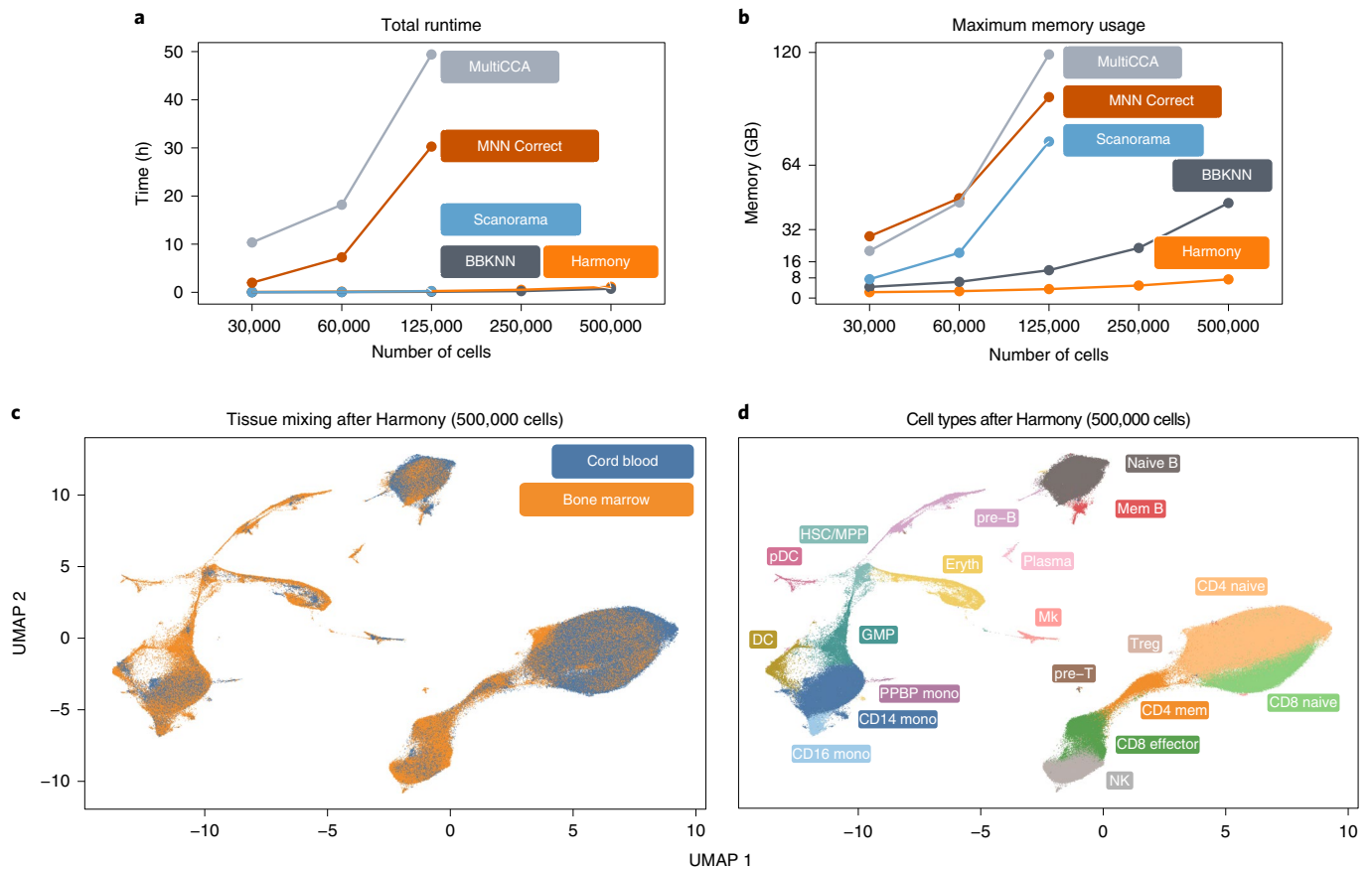
Fig. 3 | Computational efficiency benchmarks. BBKNN, Scanorama, MNN Correct and MultiCCA are compared on five downsampled HCA datasets of increasing sizes. **a,b**, Total runtime (**a**) and maximum memory (**b**) required to analyze each dataset are shown. Scanorama, MultiCCA and MNN Correct were terminated for excessive memory requests on the 250,000 and 500,000 cell datasets. **c**, The mixing between tissues in the Harmony embedding of the 500,000 cell analysis is visualized here. This includes $n = 239,794$ cells from cord blood of $n = 8$ independent donors and $n = 260,206$ cells from bone marrow of $n = 8$ independent donors. **d**, In the Harmony embedding, clustered cell populations are labeled by canonical markers: pre-T cells, CD4 naive T cells, CD4 memory T cells, T-regs, CD8 naive T cells, CD8 effector T cells, NK cells, pre-B cells, naive B cells, memory B cells, plasma cells, plasmacytoid dendritic cells (pDC), conventional dendritic cells (DC), granulocyte macrophage progenitor (GMP), CD16$^-$ monocytes (CD14 mono), CD16$^+$ monocytes (CD16 mono), a population of monocytes also positive for megakaryocyte markers (PPBP mono), megakaryocytes (Mk), erythroid progenitors (Eryth) and a cluster of hematopoietic stem cells and multipotent progenitor cells (HSC/MPP).

dataset, we separately annotated (Methods) broad cell clusters with canonical markers of major expected populations (Supplementary Fig. 6d): monocytes (CD14$^+$ or CD16$^+$), dendritic cells (FCER1A$^+$), B cells (CD20$^+$), T cells (CD3$^+$), megakaryocytes (PPBP$^+$) and natural killer (NK) cells (CD3$^-$/GNLY$^+$) before clustering. We observed that Harmony (median cLISI 1.00, 95% CI [1.00, 1.15]) retained differences among cell types, similar to other integration methods (median cLISI 1.00, 95% CI [1.00, 1.28]). The greater dataset integration, compared to other algorithms, affords a unique opportunity to identify fine-grained cell subtypes (Supplementary Fig. 6e). Using canonical markers (Fig. 4e), we identified shared subpopulations of cells (Fig. 4f) including naive CD4 T (CD4$^+$/CCR7$^+$), effector memory CD4 T (CD4$^+$/CCR7$^-$), Treg (CD4$^+$/FOXP3$^+$), memory CD8 (CD8$^+$/GZMK$^-$), effector CD8 T (CD8$^+$/GZMK$^+$), naive B (CD20$^+$/CD27$^-$) and memory B cells (CD20$^+$/CD27$^+$). In the embeddings produced by other algorithms, the median iLISI failed to exceed 1.1 (Supplementary Table 5). Accordingly, the subtypes identified above reside in dataset-specific, rather than dataset-mixed clusters (Supplementary Fig. 7). We were able to maintain high quality results even as we downsampled whole populations of cells to create imbalanced datasets with nonoverlapping cell types (Supplementary Results and Supplementary Figs. 8–10). In both the full and downsampled PBMC datasets, Harmony was

robust to the choice of parameters, particularly the diversity penalty (Supplementary Results and Supplementary Fig. 11). These results show that Harmony successfully accounts for technical variation among different protocols and integrates many different cell types while preserving large-scale and fine-grained structures in the data, even with nonoverlapping populations among datasets.

Simultaneous integration across donors and technologiesidentifies rare pancreas islet subtypes. We considered a more complex experimental design, in which integration must be performed simultaneously over more than one source of variation. We gathered human pancreatic islet cells from five independent studies[13–17], each generated with a different technological platform. Integration across these platforms is particularly challenging because of the large spread in number of cells per dataset and number of unique genes measured in each cell (Supplementary Fig. 12). Moreover, within two of the datasets[13,14], the authors noted considerable donor-specific effects. A successful integration of these studies must account for the effects of both different technologies and the 36 donors used in these studies. These effects may affect cell types in different ways. Harmony is the only currently available integration algorithm specifically designed for single-cell data that is able to explicitly integrate over more than one variable.
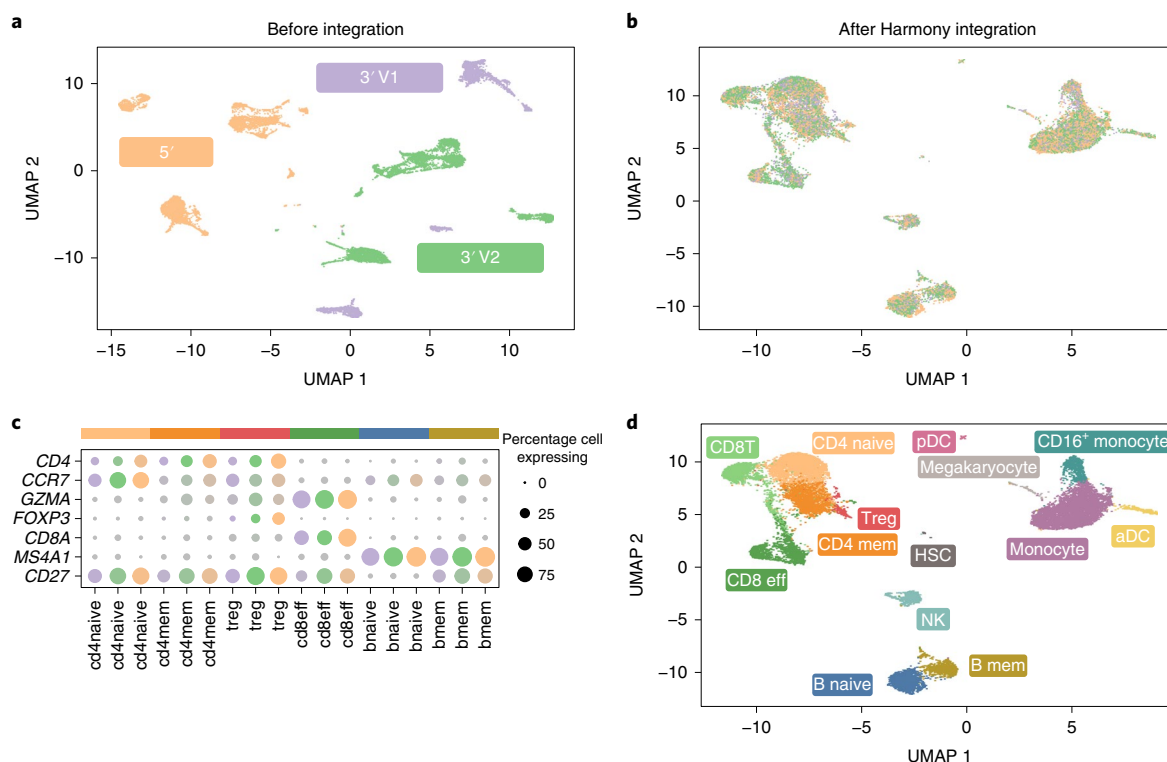
Fig. 4 | Fine-grained subpopulation identification in PBMCs across technologies. Three PBMC datasets were assayed with 10X, using different library construction protocols: 5′ (orange, $n = 7{,}697$ cells), 3′ V1 (purple, $n = 4{,}809$ cells) and 3′ V2 (green, $n = 8{,}380$ cells). **a**, Before integration, cells group by dataset. **b**, After Harmony integration, datasets are mixed together. **c,d**, Using canonical markers (**c**), we identified (**d**) five shared subtypes of T cell and two shared subtypes of B cell.

As before, we assess cell-type accuracy cLISI with canonical cell types identified independently within each dataset (Supplementary Fig. 13a): alpha (GCG$^+$), beta (MAFA$^+$), gamma (PPY$^+$), delta (SST$^+$), acinar (PRSS1$^+$), ductal (KRT19$^+$), endothelial (CDH5$^+$), stellate (COL1A2$^+$) and immune (PTPRC$^+$). Since there are two integration variables, we assess both donor iLISI and technology iLISI. Before integration, PCA separates cells by technology (Fig. 5a, median iLISI 1.00 95% CI [1.00, 1.06]), donor (Fig. 5b, median iLISI 1.42 95% CI [1.00, 5.50]) and cell type (median cLISI 1.00 95% CI [1.00, 1.48]). The wide range of donor iLISI reflects that in the CEL-seq, CEL-seq2 and Fluidigm C1 datasets, many donors were well mixed before integration. Harmony integrates cells (Supplementary Fig. 13b) by both technology (Fig. 5c, median iLISI 2.17 95% CI [1.02, 3.91]) and donor (Fig. 5d, median iLISI 5.05 95% CI [1.24, 10.05]), while merging cells correctly according to previously defined types (accuracy >98%, Supplementary Fig. 13c). We also benchmarked these data with BBKNN, Scanorama, MNN Correct and MultiCCA, as well with limma[18], which can correct over multiple levels. Only Harmony was able to mix both the donors and technologies substantially (Supplementary Results and Supplementary Fig. 14).

Harmony was able to discern rare (<2%) cell subtypes (Fig. 5e) across the five datasets (Fig. 5f). We labeled previously described subtypes using canonical markers: activated stellate cells (PDGFRA$^+$), quiescent stellate cells (RGS5$^+$), mast cells (BTK$^+$), macrophages (C1QC$^+$) and beta cells under endoplasmic reticulum (ER) stress (Fig. 5g). Beta ER stress cells may represent a dysfunctional population, marked by ER stress genes *DDIT3* (FDR $= 2.1 \times 10^{-187}$), *ATF3* (FDR $= 3.2 \times 10^{-79}$), *ATF4* (FDR $= 1.9 \times 10^{-76}$) and *PPP1R15A* (FDR $= 1.8 \times 10^{-145}$). This cluster has significantly lower expression of genes key to beta cell identity[19] and function[20]: *PDX1* (FDR $= 1.1 \times 10^{-24}$), *MAFA*

(FDR $= 4.0 \times 10^{-30}$), *INSM1* (FDR $= 3.2 \times 10^{-4}$) and *NEUROD1* (FDR $= 9.6 \times 10^{-42}$) (Fig. 5h). Further, Sachdeva et al.[21] suggest that *PDX1* deficiency makes beta cells less functional and exposes them to ER stress induced apoptosis.

We also observed an alpha cell subset that to our knowledge, has not been previously described. This cluster was also enriched with genes involved in ER stress (Fig. 5i, *DDIT3* (FDR $= 2.6 \times 10^{-29}$), *ATF3* (FDR $= 5.5 \times 10^{-55}$), *ATF4* (FDR $= 2.4 \times 10^{-74}$) and *PPP1R15A* (FDR $= 6.7 \times 10^{-113}$)). Similar to the beta ER stress population, these alpha cells also expressed significantly lower levels of genes necessary for proper function[22,23]: *GCG* (FDR $= 4.2 \times 10^{-13}$), *ISL1* (FDR $= 1.0 \times 10^{-22}$), *ARX* (FDR $= 3.8 \times 10^{-26}$) and *MAFB* (FDR $= 1.0 \times 10^{-71}$) (Fig. 5j). A recent study[24] reported ER stress in alpha cells in mice and linked the stress to dysfunctional glucagon secretion. Moreover, we found that the proportions of alpha and beta ER stress cells are significantly correlated (Spearman $r = 0.46$, $P = 0.004$, Fig. 5k) across donors in all datasets. These results suggest alpha cell injury might parallel beta cell dysfunction in humans during diabetes[25]. This rare population was nearly impossible to identify in the original studies, because it was either too rare or obscured by donor-specific variation (Supplementary Fig. 15).

Harmony integrates time course developmental trajectories. We next evaluated Harmony's ability to integrate datasets with smooth trajectories, rather than discrete cell types. We analyzed 15,875 cells from eight time points of mouse hematopoiesis[26], from E6.75 to E8.5 and mixed gastrulation. This dataset presents a new challenge to Harmony: each sample was taken at a different developmental time point. Thus, no sample has all cell types represented (Supplementary Fig. 16a). Cells initially grouped by sample ID rather than by cell type (Supplementary Fig. 16b). After Harmony integration, samples were well mixed and grouped largely by
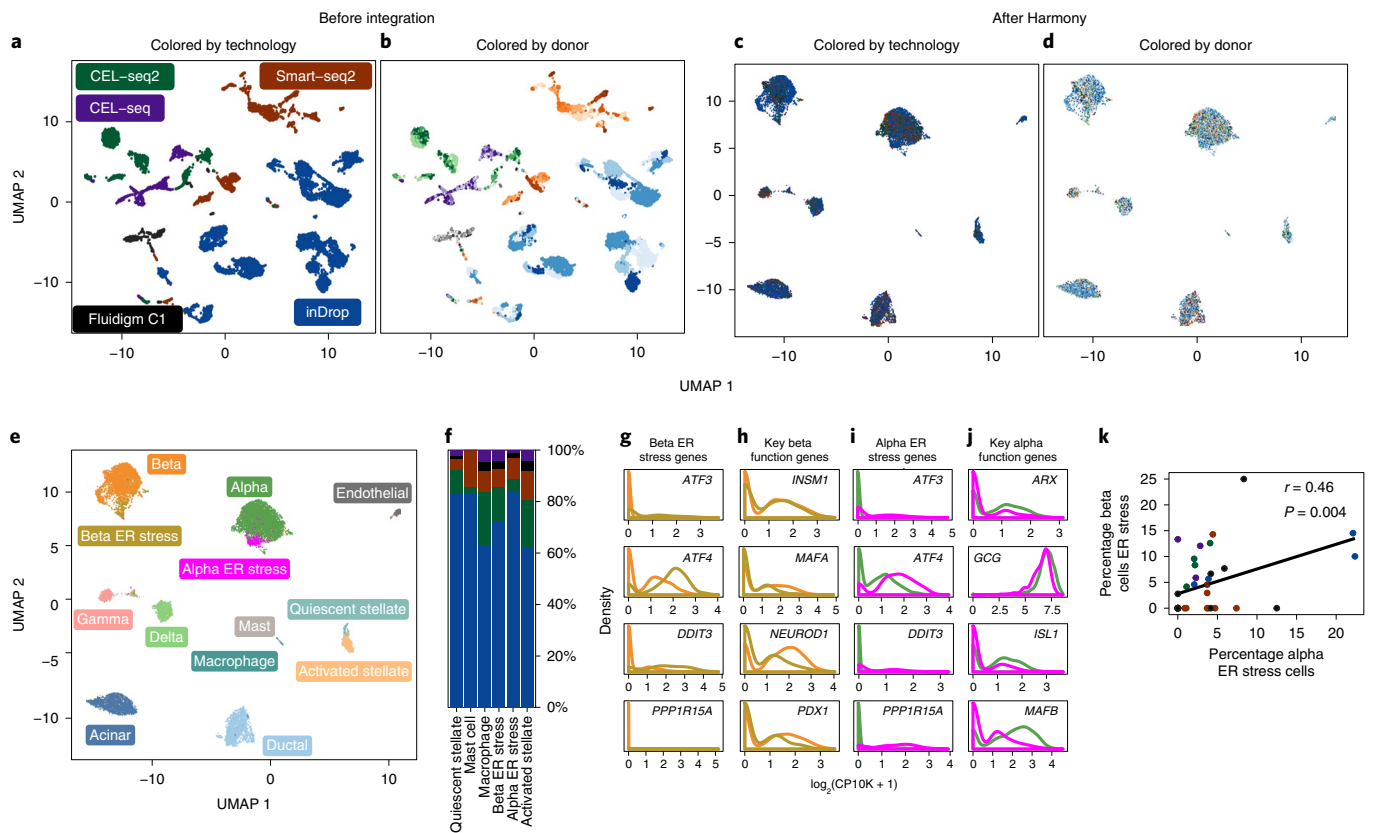
Fig. 5 | Integration of pancreatic islet cells by both donor and technology. The $n=14{,}746$ Human pancreatic islet cells from 36 donors were assayed on five different technologies: inDrop ($n=4$ donors, $n=8{,}569$ cells), Fluidigm C1 ($n=13$ donors, $n=638$ cells), Smart-Seq2 ($n=10$ donors, $n=2{,}355$ cells), CEL-seq ($n=5$ donors, $n=946$ cells) and CEL-seq2 ($n=4$ donors, $n=2{,}238$ cells). **a,b,** Cells initially group by (**a**) technology, denoted by different colors and (**b**) donor, denoted by shades of colors. **c,d,** Harmony integrates cells simultaneously across (**c**) technology and (**d**) donor. **e,** Clustering in the Harmony embedding. **f,** Proportion of the different cell types. **g,h,** We compare the log expression (normalized to counts-per-ten-thousand, CP10K) of ER stress genes (**g**) and beta endocrine function genes (**h**) in the beta ER stress cell population (green, $n=306$ cells) to that in the beta cell population (orange, $n=3{,}374$ cells). **i,j,** Similarly, we compare the expression ER stress genes (**i**) and alpha endocrine function genes (**j**) in the alpha ER stress cell population (purple, 392 cells) to the alpha cell population (green, $n=3{,}978$ cells). Differential expression analysis was performed with two-tailed moderated t-tests. FDR was computed using the Benjamini–Hochberg procedure. **k,** The abundances of the two ER stress populations were correlated across $n=36$ donors. Correlation was computed using Spearman's rho and the nomial P value estimated with algorithm AS 89. Only one test was performed, so no multiple hypothesis correction was applied.

previously defined cell type (Supplementary Fig. 16c). Harmony preserved the continuous structure of the developmental cells rather than erroneously clustering cells into discrete groups. Harmony's soft clustering was critical to preserve the smoothness: it assigned cells from transitional populations to more clusters and cells in more terminal populations to fewer clusters (Supplementary Fig. 16d). With corrected Harmony embeddings, we performed trajectory analysis with DDRTree (Supplementary Fig. 16e). We recovered a branching trajectory structure that correctly captures the progression from common mesoderm and hematoendothelial progenitor populations to differentiated endothelial and erythroid populations. Harmony preserved the separation between the two blood progenitor populations but not in the three erythroid populations (Supplementary Fig. 16e). This suggests that these distinct erythroid populations may be an artifact of batch rather than biology. Benchmarking this analysis, (Supplementary Results), we found that except for MNN Correct, other algorithms failed to maintain smoothness or incorrectly mixed distinct progenitor populations (Supplementary Fig. 17).

Harmony integrates dissociated scRNAseq with spatially resolved datasets. Now we consider the integration of cells measured with different modalities, measuring different aspects of

a cell's biology. This type of integration is especially powerful, in that it allows inference of features measured in one modality but not the other. Harmony integrates a spatially resolved multiplexed error robust fluorescence in situ hybridization (MERFISH) dataset with a dissociated scRNAseq dataset from the mouse hypothalamic preoptic region (Bregma +0.5 to −0.6 mm), using 154 shared genes (Fig. 6a). From the embedding, we infer the spatial localization of unmeasured genes to identify previously unreported spatial patterns in neuronal transcription factors. We downloaded two datasets published by Moffit et al.[27,28]: 30,370 cells from six mice measured with dissociated scRNAseq (10×) and 64,373 cells from one mouse measured with MERFISH. The spatially resolved dataset is a combination of 135 genes assayed with MERFISH and 20 assayed with two-color single molecule FISH (smFISH). The dissociated 10× data gives information about the full transcriptome (22,067 genes post quality control) but without any spatial information. In contrast, MERFISH was applied in this dataset to only a targeted number of genes. The primary challenge in this analysis is the limited number of overlapping features. Successful integration will merge similar cell types and allow inference of spatial patterns of the remaining 21,913 genes.

Before Harmony, cells group primarily by modality (median iLISI 1.00, 95% CI [1.00, 1.04], see Supplementary Fig. 18a). Harmony
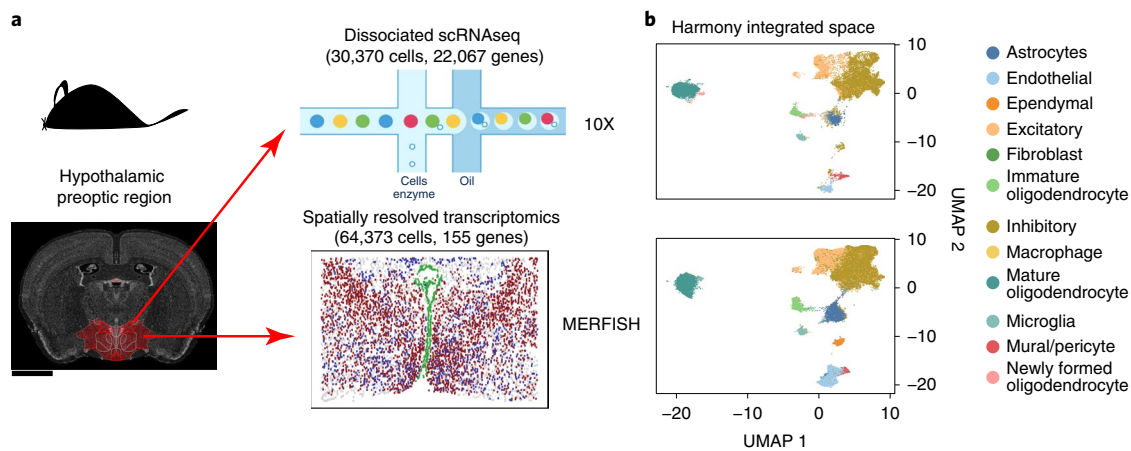
Fig. 6 | Harmony integrates spatially resolved transcriptomic with dissociated scRNAseq datasets. a, Cells from the hypothalamic preoptic region of mouse brain were assayed in parallel with two technologies. The full transcriptome of $n = 30{,}370$ dissociated cells from $n = 6$ animals was profiled with 10X. 155 genes were profiled in situ for $n = 64{,}373$ cells from $n = 1$ animal on intact tissue with MERFISH. Scale bar, 2 mm. **b,** Harmony integrated cells from the two modalities into a shared embedding, correctly merging the 12 previously identified cell types.

mixes the two modalities, 10× and MERFISH (median iLISI 1.15, 95% CI [1.00, 1.99], see Fig. 6b and Supplementary Fig. 18b) and merges cells based on their previous cell-type labels, covering 12 major neuronal and glial populations (93.7% prediction accuracy after integration versus 94% before integration, see Supplementary Fig. 18c). As an independent validation, we show that the Harmony embedding agrees with the fine-grained cluster analysis in the original paper (Supplementary Results and Supplementary Fig. 18d,e).

We next used kernel k-nearest-neighbor (kNN) imputation to predict gene expression in MERFISH dataset cells, based on their nearest 10X dataset neighbors (Methods). We used fivefold cross-validation to evaluate performance and found that we predicted 150 of 154 genes accurately, performing consistently better on highly expressed genes (Supplementary Results and Supplementary Fig. 18f). The original paper identified key transcription factors that distinguished spatially distributed neuronal subtypes. After applying Harmony, we can easily identify spatially autocorrelated transcription factors. We measured the spatial autocorrelation (Moran's I) of all known vertebrate transcription factors documented in JASPAR[29] (Supplementary Tables 6 and 7). As expected, all factors associated with a neuronal subtype were significantly (FDR < 5%) spatially autocorrelated. In addition, we found 50 transcription factors significantly (FDR < 5%, Moran's I > 0.1) autocorrelated in excitatory neurons and 37 in inhibitory neurons. We confirmed that these new factors were positive markers for at least one neuronal subtype. In fact, spatial correlation was significantly correlated (Spearman's $r = 0.71$, $P = 2.6 \times 10^{-62}$) with the area under the curve of that gene's best subtype (Supplementary Fig. 18g).

We next followed up on *Satb1*, a chromatin organizer linked with survival of mouse cortical interneurons[30], as it was strongly autocorrelated in inhibitory neurons (Moran's $I = 0.44$). The predicted *Satb1* expression was localized to anterior slices (Supplementary Fig. 18h). To validate this localization, we compared predicted expression to matched images of *Satb1* expression from the Allen Brain Atlas[31]. These images were chosen for similar anterior–posterior position (between Bregma +0.8 to −0.2 mm) and ventricular morphology (in green). The measured *Satb1* expression follows qualitatively similar patterns of predicted expression.

These 154 genes were carefully selected by the authors to be biologically relevant to cell types in the hypothalamic preoptic region. Using correlation informed downsampling, we were able to achieve similar results with only 60 representative anchor genes (Supplementary Results and Supplementary Fig. 18i,j).

Discussion

Harmony accepts a matrix of cells and covariate labels for each cell as input. Its output is a matrix of adjusted coordinates with the same dimensions as the input matrix. Hence, Harmony should be applied first before a full analysis pipeline is employed. Downstream analyses, such as clustering, trajectory analysis and visualization, can then use adjusted Harmony embeddings. Harmony does not alter the expression values of individual genes to account for dataset-specific differences. We recommend using a batch-aware approach, such as mixed effects linear models, for differential expression analysis.

Harmony uses clusters to partition the large nonlinear embeddings in which cells sit into smaller linear regions. With discrete clustering, it is possible to over-discretize the space and lose smooth transitions between populations (for examples, see Supplementary Note 3). Harmony avoids over-discretization by using soft clustering. With this strategy, in the mouse embryogenesis dataset, Harmony effectively modeled both terminal populations and transition states, retaining smooth transitions and bifurcation events from a common progenitor into endothelial and hematopoietic lineages.

With the advent of high throughput single-cell technologies, it is now possible to assay different interacting facets of a cell's biology. Effective synthesis of datasets across multiple modalities may help reveal such interactions. Harmony embedded spatially resolved MERFISH cells with dissociated 10× cells, despite limited overlap of genes and dramatically different detection efficiencies between these technologies. Consequently, we were able to analyze spatial patterns of gene expression on genes that were never measured with MERFISH. The ability of Harmony to integrate 10X and MERFISH and impute unmeasured gene expression relies on the quality of the overlapping set of anchor genes. Selecting the optimal anchor genes is an important open question. From our cross-validation and minimal gene set analyses, we found two trends that may help guide spatial probeset design. First, we can remove correlated genes from the anchors with minimal loss in integration quality. Second, less abundant genes are more difficult to predict. Thus, a spatial probeset containing genes with lower abundance that are also maximally nonredundant should enable imputation of a large number of genes through Harmony with an appropriately matched scRNAseq dataset.

It is common practice to apply batch-sensitive gene preprocessing steps before application of single-cell integration algorithms. In particular, some investigators scale gene expression values

within datasets separately, before pooling cells into a single matrix. While this strategy may make it easier to integrate certain datasets (Supplementary Results and Supplementary Fig. 19a,b) in which all cell populations are present across all datasets, it may increase error when datasets consist of overlapping but not identical populations (Supplementary Fig. 19c). Hence, we do not use this scaling strategy in this article. In our analysis pipelines, we avoid all batch-sensitive preprocessing steps. We simply concatenate the data and perform PCA on the combined dataset.

Harmony models and removes the effects of known sources of variation. However, unwanted variation may also arise from unknown sources. Methods such as SVA[32] and PEER[33] infer and remove latent sources of variation with linear models in bulk transcriptomics. In future work, we plan to extend Harmony to identify and remove unwanted latent effects.

With the rise of automated classification algorithms, it is feasible that a user may be able to assign information about cell types before integration. For example, in the past, our group has used a classifier to define soft or hard identities to assign probabilistic classifications to single cells with linear discriminant analysis[3,34]. Harmony has an advanced option to initialize soft cluster assignments using such probabilistic cell-type assignments (see HarmonyMatrix). If the previous assignments are helpful, Harmony will converge to an accurate solution faster. If the previous assignments are inaccurate, Harmony can reassign cells appropriately during the clustering steps.

The Harmony framework lays the groundwork for several exciting future applications. First, it can be extended to accurately model gene counts. This will allow users to apply Harmony preprocessing for methods that require full gene expression profiles, rather than low-dimensional cell embeddings, such as RNA velocity[35]. Next, we envision specializing Harmony to quickly map cells to a multi-billion cell reference that covers a comprehensive set of tissues, organisms and clinical conditions. This application will enable rapid comparison of cells from a single experiment against a larger reference, and in the process annotate known and new cell types and states in seconds.

Online content

Any methods, additional references, Nature Research reporting summaries, source data, extended data, supplementary information, acknowledgments, peer review information, details of author contributions and competing interests, and statements of code and data availability are available at https://doi.org/10.1038/s41592-019-0619-0.

References
1. Svensson, V., Vento-Tormo, R. & Teichmann, S. A. Exponential scaling of single-cell RNA-seq in the past decade. *Nat. Protocols* **13**, 599–604 (2018).
2. Regev, A. et al. The human cell atlas. *eLife* **6**, e27041 (2017).
3. Zhang, F. et al. Defining inflammatory cell states in rheumatoid arthritis joint synovial tissues by integrating single-cell transcriptomics and mass cytometry. *Nat. Immunol.* **20**, 928–942 (2019).
4. Arazi, A. et al. The immune cell landscape in kidneys of lupus nephritis patients. *Nat. Immunol.* **20**, 902–914 (2019).
5. Der, E. et al. Tubular cell and keratinocyte single-cell transcriptomics applied to lupus nephritis reveal type I IFN and fibrosis relevant pathways. *Nat. Immunol.* **20**, 915–927 (2019).
6. Hicks, S. C., Townes, F. W., Teng, M. & Irizarry, R. A. Missing data and technical variability in single-cell RNA-sequencing experiments. *Biostatistics* **19**, 562–578 (2017).
7. Butler, A., Hoffman, P., Smibert, P., Papalexi, E. & Satija, R. Integrating single-cell transcriptomic data across different conditions, technologies, and species. *Nat. Biotechnol.* **36**, 411–420 (2018).
8. Haghverdi, L., Lun, A. T. L., Morgan, M. D. & Marioni, J. C. Batch effects in single-cell RNA-sequencing data are corrected by matching mutual nearest neighbors. *Nat. Biotechnol.* **36**, 421–427 (2018).
9. Hie, B. L., Bryson, B. & Berger, B. Efficient integration of heterogeneous single-cell transcriptomes using Scanorama. *Nat. Biotechnol.* **37**, 685–691 (2018).
10. Polanski, K. et al. BBKNN: fast batch alignment of single cell transcriptomes. *Bioinformatics* https://doi.org/10.1093/bioinformatics/btz625 (2019).
11. Zheng, G. X. Y. et al. Massively parallel digital transcriptional profiling of single cells. *Nat. Commun.* **8**, 14049 (2017).
12. Li, B. et al. *HCA Data Portal: census of immune cells* (Human Cell Atlas, 2019).
13. Segerstolpe, Å. et al. Single-cell transcriptome profiling of human pancreatic islets in health and type 2 diabetes. *Cell Metab.* **24**, 593–607 (2016).
14. Baron, M. et al. A single-cell transcriptomic map of the human and mouse pancreas reveals inter- and intra-cell population structure. *Cell Syst.* **3**, 346–360 (2016).
15. Lawlor, N. et al. Single-cell transcriptomes identify human islet cell signatures and reveal cell-type-specific expression changes in type 2 diabetes. *Genome Res.* **27**, 208–222 (2017).
16. Grun, D. et al. De novo prediction of stem cell identity using single-cell transcriptome data. *Cell Stem Cell* **19**, 266–277 (2016).
17. Muraro, M. J. et al. A single-cell transcriptome atlas of the human pancreas. *Cell Syst.* **3**, 385–394 (2016).
18. Ritchie, M. E. et al. Limma powers differential expression analyses for RNA-sequencing and microarray studies. *Nucleic Acids Res.* **43**, e47 (2015).
19. Gao, T. et al. Pdx1 maintains β cell identity and function by repressing an α cell program. *Cell Metab.* **19**, 259–271 (2014).
20. Jia, S. et al. Insm1 cooperates with neurod1 and foxa2 to maintain mature pancreatic β-cell function. *EMBO J.* **34**, 1417–1433 (2015).
21. Sachdeva, M. M. et al. Pdx1 (MODY4) regulates pancreatic beta cell susceptibility to ER stress. *Proc. Natl Acad. Sci. USA* **106**, 19090–19095 (2009).
22. Katoh, M. C. et al. MafB is critical for glucagon production and secretion in mouse pancreatic α cells in vivo. *Mol. Cell. Biol.* **38**, e00504–e00517 (2018).
23. Liu, J. et al. Islet-1 regulates arx transcription during pancreatic islet α-cell development. *J. Biol. Chem.* **286**, 15352–15360 (2011).
24. Akiyama, M. et al. X-box binding protein 1 is essential for insulin regulation of pancreatic α-cell function. *Diabetes* **62**, 2439–2449 (2013).
25. Burcelin, R., Knauf, C. & Cani, P. D. Pancreatic alpha-cell dysfunction in diabetes. *Diabetes Metab.* **34**, S49–S55 (2008).
26. Pijuan-Sala, B. et al. A single-cell molecular map of mouse gastrulation and early organogenesis. *Nature* **566**, 490–495 (2019).
27. Moffitt, J. R.et al. Molecular, spatial, and functional single-cell profiling of the hypothalamic preoptic region. *Science* **362**, eaau5324 (2018).
28. Moffitt, J. et al. *Data from: Molecular, Spatial and Functional Single-cell Profiling of the Hypothalamic Preoptic Region* (Dryad, Dataset, 2018); https://doi.org/10.5061/dryad.8t8s248
29. Khan, A. et al. JASPAR 2018: update of the open-access database of transcription factor binding profiles and its web framework. *Nucleic Acids Res.* **46**, D260–D266 (2018).
30. Close, J. et al. Satb1 is an activity-modulated transcription factor required for the terminal differentiation and connectivity of medial ganglionic eminence-derived cortical interneurons. *J. Neurosci.* **32**, 17690–17705 (2012).
31. Lein, E. S. et al. Genome-wide atlas of gene expression in the adult mouse brain. *Nature* **445**, 168–176 (2007).
32. Leek, J. T. & Storey, J. D. Capturing heterogeneity in gene expressionstudies by surrogate variable analysis. *PLoS Genet.* **3**, e161 (2007).
33. Stegle, O., Parts, L., Piipari, M., Winn, J. & Durbin, R. Using probabilistic estimation of expression residuals (PEER) to obtain increased power and interpretability of gene expression analyses. *Nature Protocols* **7**, 500–507 (2012).
34. Mizoguchi, F. et al. Functionally distinct disease-associated fibroblast subsets in rheumatoid arthritis. *Nat. Commun.* **9**, 789 (2018).
35. Manno, G. L. et al. RNA velocity of single cells. *Nature* **560**, 494–498 (2018).

Methods

Harmony. *Overview.* The Harmony algorithm inputs a PCA embedding (Z) of cells, along with their batch assignments (ϕ), and returns a batch corrected embedding ($\hat{Z}$). This algorithm, summarized as Algorithm 1 below, iterates between two complementary stages: maximum diversity clustering (Algorithm 2) and a mixture model based linear batch correction (Algorithm 3). The clustering step uses the batch corrected embedding $\hat{Z}$ to compute a soft assignment of cells to clusters, encoded in the matrix R. The correction step uses these soft clusters to compute a new corrected embedding from the original one. Efficient implementations of Harmony, including the clustering and correction subroutines, are available as part of an R package at https://github.com/immunogenomics/harmony.

Note that the correction procedure uses Z, not $\hat{Z}$ to regress out confounder effects. In this way, we restrict correction to a linear model of the original embedding. An alternative approach would use the output $\hat{Z}$ of the last iteration as input to the correction procedure. Thus, the final $\hat{Z}$ would be the result of a series of linear corrections of the original embedding. While this allows for more expressive transformations, we found that in practice, this can over correct the data. Our choice to limit the transformation reflects the notion in the introduction. Namely, if we had perfect knowledge of the cell types before correction, we would linearly regress out batch within each cell type.

Algorithm 1 Harmony
 function HARMONIZE (Z, ϕ)
  $\hat{Z} \leftarrow Z$
  repeat
   $R \leftarrow$ CLUSTER $(\hat{Z}, \phi)$
   $\hat{Z} \leftarrow$ CORRECT (Z, R, ϕ)
  until convergence
  return $\hat{Z}$

Glossary. For reference, we define all data structures used in all Harmony functions. For each one, we define its dimensions and possible values, as well as an intuitive description of what it means in context. The dimensions are stated in terms of d, the dimensionality of the embedding (for example, number of PCs); B, the number of batches; N, the number of samples; N_b, the number of samples in batch b; and K, the number of clusters.

$Z \in \mathbb{R}^{d \times N}$ The input embedding, to be corrected in Harmony. This is often PCA embeddings of cells.
$\hat{Z} \in \mathbb{R}^{d \times N}$ The integrated embedding, output by Harmony.
$R \in [0,1]^{K \times N}$ The soft cluster assignment matrix of cells (columns) to clusters (rows). Each column is a probability distribution and thus sums to 1.
$\phi \in \{0,1\}^{B \times N}$ One-hot assignment matrix of cells (columns) to batches (rows).
$\text{Pr}_b \in [0,1]^B$ Frequency of batches.
$O \in [0,1]^{K \times B}$ The observed co-occurence matrix of cells in clusters (rows) and batches (columns).
$E \in [0,1]^{K \times B}$ The expected co-occurence matrix of cells in clusters and batches, under the assumption of independence between cluster and batch assignment.
$Y \in [0,1]^{d \times K}$ Cluster centroid locations in the k-means clustering algorithm.

Assumptions about input data. In this article, we always use Harmony on a low-dimensional embedding of the cells. To be clear about the properties of this low-dimensional space, we explicitly state three assumptions:

1. Cells are embedded into a low-dimensional space as the result of PCA. The PCA embedding captures the variation of gene expression in a compact orthonormal space. For this reason, the default input to Harmony is now a matrix of gene expression data, normalized for library size. We then perform PCA on this high-dimensional matrix and use the eigenvalue-scaled eigenvectors as the low-dimensional embedding input to Harmony.

2. Gene expression has been normalized for library size. In RNA-seq, each cell will be sequenced to a different depth, which results in different library sizes for each cell. It is best practice to account for this source of technical variation before performing PCA. In this article, we use the standard log counts-per-10,000 (CP10K) transformation, described in the Methods. As a result of this depth transformation, expression values are turned into relative frequencies inside each cell. Thus, it is impossible for every gene to be upregulated in one group of cells.

3. The low-dimensional nearest-neighbor structure induced by Euclidean distance should be preserved with common similarity metrics such as cosine similarity and correlation. This can be easily checked by computing sparse nearest-neighbor graphs and comparing the adjacency matrices. Cells with less than 20% overlapping neighbors can be removed as outliers. A common way to violate this assumption is to simulate cells around the origin (that is, all embeddings equal 0). We do not find this to be the case in real scRNAseq data. This assumption is common to integration methods that use cosine distance to compare cells, such as MNN Correct and Scanorama.

Maximum diversity clustering. We developed a clustering algorithm to maximize the diversity among batches within clusters. We present this method as follows.

First, we review a previously published objective function for soft k-means clustering. We then add a diversity maximizing regularization term to this objective function, and derive this regularization term as the penalty on statistical dependence between two random variables: batch membership and cluster assignment. We then derive and present pseudocode for an algorithm to optimize the objective function. Finally, we explain key details of the implementation.

Background: entropy regularization for soft k-means. The basic objective function for classical k-means clustering, in which each cell belongs to exactly one cluster, is defined by the distance from cells to their assigned centroids.

$$\min_{R,Y} \sum_{i,k} R_{ki} \|Z_i - Y_k\|^2 \tag{1}$$

$$\text{s.t.} \forall_i \forall_k \, R_{ki} \in \{0,1\}$$

Above, Z is some feature space of the data, shared by centroids Y. $R_{k,i}$ can take values 0 or 1, denoting membership of cell i in cluster k. To transform this into a soft clustering objective, we follow the direction of ref. [36] and add an entropy regularization term over R, weighted by a hyperparameter σ. Now, R_{ki} can take values between 0 and 1, so long as for a given cell i, the sum over cluster memberships $\Sigma_k R_{ki}$ equals 1. That is, R_i must be a proper probability distribution with support $[1,K]$.

$$\min_{R,Y} \sum_{i,k} R_{ki} \|Z_i - Y_k\|^2 + \sigma R_{ki} \log R_{ki} \tag{2}$$

$$\text{s.t.} \forall_i \forall_k \, R_{ki} > 0, \forall_i \sum_{k=1}^{K} R_{ki} = 1$$

As σ approaches 0, this penalty approaches hard clustering. As σ approaches infinity, the entropy of R outweighs the data-centroid distances. In this case, each data point is assigned equally to all clusters.

Objective function for maximum diversity clustering. The full objective function for Harmony's clustering builds on the previous section. In addition to soft assignment regularization, the function below penalizes clusters with low batch-diversity, for all defined batch variables. This penalty, derived in the following section, depends on the cluster and batch identities $\Omega(R, \phi_i) = \Sigma_{i,k} R_{ki} \log(O_{ki}/E_{ki}) \phi_i$.

$$\min_{R,Y} \sum_{i,k} R_{ki} \|Z_i - Y_k\|^2 + \sigma R_{ki} \log R_{ki} + \sigma \theta R_{ki} \log\left(\frac{O_{ki}}{E_{ki}}\right) \phi_i \tag{3}$$

$$\text{s.t.} \forall_i \forall_k \, R_{ki} > 0, \forall_i \sum_{k=1}^{K} R_{ki} = 1$$

For each batch variable, we add a new parameter θ. Here θ decides the degree of penalty for dependence between batch membership and cluster assignment. When $\forall_f \theta = 0$, the problem reverts back to (2), with no penalty on dependence. As θ increases, the objective function favors more independence between batch f and cluster assignment. As θ approaches infinity, it will yield a degenerate solution. In this case, each cluster has an equivalent distribution across batch f. However, the distances between cells and centroids may be large. Finally, σ is added to this term for notational convenience in the gradient calculations.

We found that this clustering works best when we compute the cosine, rather than Euclidean distance, between Z and Y. Haghverdi et al.[8] showed that the squared Euclidean distance is equivalent to cosine distance when the vectors are $\log_2$ normalized. Therefore, assuming that all Z_i and Y_k have a unity $\log_2$ norm, the squared Euclidean distance above can be re-written as a dot product.

$$\min_{R,Y} \sum_{i,k} R_{ki} 2 \left(1 - Y_k^T Z_i\right) + \sigma R_{ki} \log R_{ki} + \sigma \theta R_{ki} \log\left(\frac{O_{ki}}{E_{ki}}\right) \phi_i \tag{4}$$

$$\text{s.t.} \forall_i \forall_k R_{ki} > 0, \forall_i \sum_{k=1}^{K} R_{ki} = 1$$

Cluster diversity score. Here, we discuss and derive the diversity penalty term $\Omega(.)$, defined in the previous section. For simplicity, we discuss diversity with respect to a single batch variable, as the multiple batch penalty terms are additive in the objective function. The goal of $\Omega(.)$ is to penalize statistical dependence between batch identity and cluster assignment. In statistics, dependence between two discrete random variables is typically measured with the χ^2 statistic. This test considers the frequencies with which different values of the two random variables are observed together. The observed co-occurrence counts (O) are compared to the counts expected under independence (E). For practical reasons, we do not use

the χ^2 statistic directly. Instead, we use the Kullback Leibler divergence (D_{KL}), an information theoretic distance between two distributions. In this section, we define the O and E distributions, as well the D_{KL} penalty, in the context of the probabilistic cluster assignment matrix R.

$$O_{kb} = N\Pr(k, b)$$

$$O_{kb} = N\Pr(k|b)\Pr(b)$$

$$O_{kb} = N\left(\sum_i 1_{i \in b} \frac{R_{ki}}{N_b}\right)\frac{N_b}{N}$$

$$O_{kb} = \sum_i 1_{i \in b} R_{ki} \tag{5}$$

$$E_{kb} = N\Pr(k, b)$$

$$E_{kb} = N\Pr(k)\Pr(b)$$

$$E_{kb} = N\left(\sum_i \frac{R_{ki}}{N_b}\right)\frac{N_b}{N}$$

$$E_{kb} = \frac{N_b}{N}\sum_i R_{ki} \tag{6}$$

Next, we define the KL divergence in terms of R. Note that both O and E depend on R. However, in the derivation below, we expand one of the O terms. This serves a functional purpose in the optimization procedure, described later. Intuitively, in the update step of R for a single cell, we compute O and E on all the other cells. In this way, we decide how to assign the single cell to clusters given the current distribution of batches among ation clusters.

$$D_{KL}(E||O) = \sum_{b=1}^{B}\sum_{k=1}^{K} O_{bk}\log\left(\frac{O_{kb}}{E_{kb}}\right)$$

$$D_{KL}(E||O) = \sum_{b=1}^{B}\sum_{k=1}^{K}\left[\sum_{i=1}^{N} 1_{i \in b} R_{ki}\right]\log\left(\frac{O_{kb}}{E_{kb}}\right)$$

$$D_{KL}(E||O) = \sum_{i=1}^{N}\sum_{k=1}^{K}\sum_{b=1}^{B} 1_{i \in b} R_{ki}\log\left(\frac{O_{kb}}{E_{kb}}\right)$$

$$D_{KL}(E||O) = \sum_{i=1}^{N}\sum_{k=1}^{K} R_{ki}\log\left(\frac{O_{kb}}{E_{kb}}\right)\phi_i \tag{7}$$

Optimization. Optimization of equation (4) admits an expectation-maximization framework, iterating between cluster assignment (R) and centroid (Y) estimation.

Cluster assignment R. Using the same strategy as ref. [36], we solve for the optimal assignment R_i for each cell i. First, we set up the Lagrangian with dual parameter λ and solve for the partial derivative with respect to each cluster k.

$$L(R_i, \lambda) = \sum_{k=1}^{K} R_{ki}2(1 - Y_k^T Z_i) + \sigma R_{ki}\log R_{ki} + \sigma\theta R_{ki}\log\left(\frac{O_{ki}}{R_{ki}}\right)$$
$$+ \lambda\left[\left(\sum_{k=1}^{K} R_{ki}\right) - 1\right]$$

$$\frac{\delta L(R_i, \lambda)}{\delta R_{ki}} = 0 = 2(1 - Y_k^T Z_i) + \sigma + \sigma\log R_{ki} + \sigma\theta\log\left(\frac{O_{ki}}{E_{ki}}\right) + \lambda$$

$$\log R_{ki} = -\frac{2(1 - Y_k^T Z_i)}{\sigma} - 1 - \theta\log\left(\frac{O_{ki}}{E_{ki}}\right) - \frac{\lambda}{\sigma}$$

$$R_{ki} = \left(\frac{O_{ki}}{E_{ki}}\right)^\theta \exp\left(-\frac{2(1 - Y_k^T Z_i)}{\sigma}\right)\exp\left(-\frac{\lambda}{\sigma} - 1\right)$$

Next, we use the probability constraint $\sum_{k=1}^{K} R_{ki} = 1$ to solve for $\exp(\lambda/\sigma - 1)$.

$$1 = \sum_{k=1}^{K} R_{ki}$$

$$1 = \sum_{k=1}^{K}\left(\frac{O_{ki}}{E_{ki}}\right)^\theta \exp\left(-\frac{2(1 - Y_k^T Z_i)}{\sigma}\right)\exp\left(-\frac{\lambda}{\sigma} - 1\right)$$

$$\exp\left(-\frac{\lambda}{\sigma} - 1\right) = \frac{1}{\sum_{k=1}^{K}\left(\frac{O_{ki}}{E_{ki}}\right)^\theta \exp\left(-\frac{2(1 - Y_k^T Z_i)}{\sigma}\right)}$$

Finally, we substitute $\exp(\lambda/\sigma - 1)$ to remove the dependency of R_{ki} on the dual parameter λ.

$$R_{ki} = \frac{\left(\frac{O_{ki}}{E_{ki}}\right)^2 \exp\left(-\frac{2(1 - Y_k^T Z_i)}{\sigma}\right)}{\sum_{k=1}^{K}\left(\frac{O_{ki}}{E_{ki}}\right)^2 \exp\left(-\frac{2(1 - Y_k^T Z_i)}{\sigma}\right)} \tag{8}$$

The denominator term above makes sure that R_i sums to one. In practice (Algorithm 2), we compute the numerator and divide by the sum.

Centroid estimation Y. Our clustering algorithm uses cosine distance instead of Euclidean distance. In the context of k-means clustering, this approach was pioneered by Dhillon et al.[37]. We adopt their centroid estimation procedure for our algorithm. Instead of just computing the mean position of all cells that belong in cluster k, this approach then $\log_2$ normalizes each centroid vector to make it unit length. Note that normalizing the sum over cells is equivalent to normalizing the mean of the cells. In the soft clustering case, this summation is an expected value of the cell positions, under the distribution defined by R. That is, re-normalizing R_k for cluster k gives the probability of each cell belonging to cluster k. Again, this re-normalization is a scalar factor that is irrelevant once we $\log_2$ normalize the centroids. Thus, the unnormalized expectation of centroid position for cluster k would be $Y_k = \mathbb{E}_{R_k} Z = \Sigma_i R_{ki} Z_i$. In vector form, for all centroids, this is $Y = ZR^T$. The final position of the cluster centroids is given by this summation followed by $\log_2$ normalization of each centroid. This procedure is implemented in Algorithm 2 in the section {*Compute Cluster Centroids*}.

Algorithm 2 Maximum Diversity Clustering
function CLUSTER $(\hat{Z}, \phi)$
    {*Initialize Cluster Centroids*}
    $Y \leftarrow kmeans(\hat{Z}, K)$
    for $i \leftarrow 1...N$ **do**   ▷ L_2 Normalization
        $Y_{\cdot,i} \leftarrow Y_{\cdot,i}/\|Y_{\cdot,i}\|_2$
        $\hat{Z}_{\cdot,i} \leftarrow \hat{Z}_{\cdot,i}/\|\hat{Z}_{\cdot,i}\|_2$
    $E \leftarrow R1Pr_b^T$
    $O \leftarrow R\phi^T$

    repeat
        for all Update Blocks **do**
            $in \leftarrow$ cells to update in block
            {*Compute O and E on left out data*}
            $E \leftarrow E - R_{in}1Pr_b^T$
            $O \leftarrow O - R_{in}\phi_{in}^T$

            {*Update and Normalize R*}
            $R_{in} \leftarrow \exp\left(-\frac{2(1 - Y^T Z_{in})}{\sigma}\right)$
            $\Omega \leftarrow (E + 1/O + 1)^\theta \phi_{in}$
            $R_{in} \leftarrow R_{in} \circ \Omega$
            $R_{in} \leftarrow R_{in} \cdot diag(1^T R_{in})^{-1}$ ▷ R_i sum to one

            {*Compute O and E with full data*}
            $E \leftarrow E + R_{in}1Pr_b^T$
            $O \leftarrow O + R_{in}\phi_{in}^T$

w   {*Compute Cluster Centroids*}
        $Y \leftarrow ZR^T$
        for $i \leftarrow 1...N$ **do**   ▷ L_2 Normalization
            $Y_{\cdot,i} \leftarrow Y_{\cdot,i}/\|Y_{\cdot,i}\|_2$
    until convergence
    return R

Implementation details. The update steps of R and Y derived above form the core of maximum diversity clustering, outlined as Algorithm 2. This section explains the other implementation details of this pseudocode. Again, for simplicity, we discuss details related to diversity penalty terms θ, ϕ, O and E for each single batch variable independently.

Block updates of R. Unlike in regular k-means, the optimization procedure above for R cannot be faithfully parallelized, as the values of O and E change with R. The exact solution therefore depends an online procedure. For speed, we can coarse grain this procedure and update R in small blocks (for example, 5% of the data). Meanwhile, O and E are computed on the held out data. In practice, this approach succeeds in minimizing the objective for sufficiently small block size. In the algorithm, these blocks are included as the Update Blocks in the for loop.

Centroid initialization. We initialize cluster centroids using regular k-means clustering, implemented in the base R k-means function. We use ten random restarts and keep the best one. We then $\log_2$ normalize the centroids to prepare them for spherical k-means clustering in Algorithm 2, maximum diversity clustering.

Regularization for smoother penalty. The diversity penalty term $(E_{bk}/O_{bk})^\theta$ can tend toward infinity if there are no cells from batch b assigned to cluster k. This extreme penalty can erroneously force cells into an inappropriate cluster. To protect against this, we add 1 to O and E to ensure that the fraction is stable: $\left(\frac{1+E_{bk}}{1+O_{bk}}\right)$

θ discounting. The diversity penalty, weighted by θ enforces an even mixing of cells from a batch among all clusters. This assumption is more likely to break for a batch with few cells. The smaller the batch, the more likely it is, through a sampling argument, that some cell types are not represented in the batch. Spreading such a batch across all clusters would result in erroneous clustering. To prevent such a situation, we allot each batch its own θ_b term, scaled to the number of cells in the batch.

$$\theta_b = \theta_{\max}\left[1 - \exp\left(-\frac{N_b}{K\tau}\right)^2\right]$$

Above, $\theta_{\max}$ is the nondiscounted θ value, for a large enough batch. The multiplicative factor $\left[1 - \exp(-N_b/K\tau)^2\right]$ ranges from 0 to 1. This factor scales exponentially for small values of batch size N_b and plateaus for sufficiently large N_b. The hyperparameter τ can be interpreted as the minimum number of cells that should be assigned to each cluster from a single batch. By default, we use values between $\tau = 5$ and $\tau = 20$.

K, the number of clusters. The number of clusters K used in Harmony soft clustering should be set to a value that reflects the size and complexity of the dataset. Too few clusters will not capture the number of biologically distinct cell types and states. Too many clusters will give too much weight to batch-specific outliers and prevent effective integration. As a heuristic, we assume that the datasets have at most 100 distinct cell types and that each cluster should have at least 30 cells. We set the default number of clusters, K, to lie between these two extremes, for N cells.

$$K = \min\left(100, \frac{N}{30}\right)$$

Linear mixture model correction. In this section, we refer to all effects to be integrated out of the original embedding as batch effects. This does not indicate that these effects are purely technical. This terminology is only meant for convenience.

Mixture of experts model. Once we define batch-diverse clusters, we would like to remove batch-specific variation from each cluster. We achieve this with a variation on the original mixture of experts model by Jordan and Jacobs[38]. In the context of Harmony, each cell is probabilistically assigned to a small set of experts. This assignment was computed previously in the clustering step. Conditioned on a cluster/expert, mixture of experts assumes a linear relationship between the response and independent variables. Thus, we condition on cluster/expert k and define a Gaussian probability distribution for the response variables.

$$Z_i|\{\phi_i^*, R_i = k\} \approx \mathcal{N}\left(Z_i|W_k^T\phi_i^*, \sigma_k^2 I\right) \quad (9)$$

Here, the mean is a function of the independent variables ($\mu^k = W_k^T\phi_i^*$), while the covariance is not ($\sigma_k^2 I$). Note that the design matrix above (ϕ^*) is not the same as the one used in the clustering step (ϕ). We augment the original design matrix ϕ to include an intercept term: $\phi^* = 1 \| \phi$. These intercept terms capture batch-independent (that is, cell type) variation in each cluster or expert. We can also achieve more complex behavior, such as reference mapping (Reference mapping) by modifying ϕ^*.

$$\phi^* = 1\|\phi = \begin{bmatrix} 1 & \cdots & 1 \\ \phi_{11} & \cdots & \phi_{1N} \\ \vdots & \ddots & \vdots \\ \phi_{B1} & \cdots & \phi_{BN} \end{bmatrix}$$

With this generative formulation, we can solve for the parameters (W_k) of the linear model for each cluster or expert independently.

$$W_k = \left(\phi^*\mathrm{diag}(R_k)\phi^{*T}\right)^{-1}\phi^*\mathrm{diag}(R_k)Z^T \quad (10)$$

Above, $\mathrm{diag}(R_k)$ is the diagonal matrix of cluster membership terms for cluster k. Z is the matrix of original PCA embeddings

$$\mathrm{diag}(R_k) = \begin{bmatrix} R_{k1} & \cdots & 0 \\ \vdots & \ddots & \vdots \\ 0 & \cdots & R_{kN} \end{bmatrix}$$

Each column in W_k corresponds to a PC dimension, from PC$_1$ to PC$_d$. The first row of W_k corresponds to batch-independent intercept terms. The subsequent rows (1 to B) correspond to one-hot encoded batch assignments from the original design matrix ϕ.

To get the cell-specific correction values, we take the expectation of W_k with respect to the cluster assignment probability distribution R. In particular, each cell is modeled by a batch-independent intercept, represented in the first row of W_k ($W_{k[0,\cdot]}$) and its batch-dependent terms represented by the remaining rows: $W_{k[1:B,\cdot]}$.

$$Z_i = \sum_k R_{ki}\left[W_{k[0,\cdot]} + W_{k[1:B,\cdot]}^T\phi_{i[1:B]}^*\right] + \epsilon_i \quad (11)$$

We split W_k into two parts because we want to retain the intercept terms and remove the batch-dependent terms. To get the corrected embeddings ($\hat{Z}_i$), we subtract the batch-specific term ($\Sigma_k W^T_{k[1:B,\cdot]}\phi_i$) from the original embedding (Z_i).

$$\hat{Z}_i = Z_i - \sum_k R_{ki}W_{k[1:B,\cdot]}^T\phi_{i[1:B]}^* \quad (12)$$

What remains is the cell-type specific intercept $W_{k[0,\cdot]}$ and the cell-specific residual ϵ_i.

$$\hat{Z}_i = \sum_k R_{ki}W_{k[0,\cdot]} + \epsilon_i \quad (13)$$

Unfortunately, for the design matrix ϕ^*, the formulation in equation (13) does not have a solution. This is because ϕ^* is not full rank and thus $\phi^* \mathrm{diag}(R_k) \phi^{*T}$ is not invertible. This singularity arises from the fact that the sum of a one-hot encoded categorical variable is equal to the intercept. To address this colinearity, we penalize nonintercept terms in W_k with a $\log_2$ norm, akin to ridge regression. This shrinks the W_k terms to 0. Just as in ridge regression, instead of inverting ϕ^* $\mathrm{diag}(R_k) \phi^{*T}$, we invert $\phi^* \mathrm{diag}(R_k) \phi^{*T} + \lambda I$, which is not singular. The solution for W_k now becomes

$$W_k = \left(\phi^*\mathrm{diag}(R_k)\phi^{*T} + \lambda I\right)^{-1}\phi^*\mathrm{diag}(R_k)Z^T \quad (14)$$

λ is the ridge penalty hyperparameter. Larger values of λ will shrink W_k more toward 0. We adopt the strategy to set $\lambda_0 = 0$, thus not penalizing the batch-independent intercept, and $\forall_{b\in[1:B]}\lambda_b$ to be small enough to make the solution tractable. In practice, we set $\forall_{b\in[1:B]}\lambda_b = 1$. These correction steps are summarized in Algorithm 3.

Algorithm 3 Mixture of Experts Correct
   function CORRECT (Z, R, ϕ)
       $\hat{Z} \leftarrow Z$
       $\phi^* \leftarrow 1\|\phi$
       for $k \leftarrow 1\ldots K$ **do**
          $W_k = (\phi^* diag(R_k)\phi^{*T} + \lambda I)^{-1}\phi^* diag(R_k)Z^T$
          $W_{k[0,\cdot]} \leftarrow 0$
          $\hat{Z} = Z - W_k^T\phi^* diag(R_k)$
       return $\hat{Z}$

Reference mapping. In Supplementary Fig. 13, we used Harmony to map two query datasets onto a reference dataset. We achieved this by modifying ϕ^* so that batch terms for reference cells does not get modeled or corrected. For every cell i in a reference dataset, set $\phi_i^* = [1, 0, \ldots, 0]$. This makes Harmony explain cell i in terms of an intercept and nothing else. Since intercept terms do not get removed, cell i never changes its embedding (that is, $Z_i = \hat{Z}_i$).

Caveat. This section assumes the modeled data are orthogonal and each normally distributed. This is not true for the $\log_2$ normalized data used in spherical clustering. Regression in this space requires the estimation and interpolation of rotation matrices, a difficult problem. We instead perform batch correction in the unnormalized space. The corrected data $\tilde{Z}$ are then $\log_2$-normalized for the next iteration of clustering.

Performance and benchmarking. *LISI metric.* Assessing the degree of mixing during batch correction and dataset integration is an open problem. Several groups have proposed methods to quantify the diversity of batches within local neighborhoods, defined by kNN graphs, of the embedded space. Buttner et al.[39] provide a statistical test to evaluate the degree of mixing, while Azizi et al.[40] report the entropy of these distributions. Our metric for local diversity is related to these approaches, in that we start with a kNN graph. However, our approach considers two problems that these do not.

First, the metric should be more sensitive to local distances. For example, a neighborhood of 100 cells can be equally mixed among four batches. However, within the neighborhood, the cells may be clustered by batch. The second problem is one of interpretation. kBET provides a statistical test to assess the significance of mixing, but it is not clear whether all neighborhoods should be significantly mixed when the datasets have vastly different cell-type proportions. Azizi et al.[40] use entropy as a measure of diversity, but it is not clear how to interpret the number of bits required to encode a neighborhood distribution.

Our diversity score, the LISI addresses both points. To be sensitive to local diversity, we build Gaussian kernel-based distributions of neighborhoods. This gives distance-based weights to cells in the neighborhood. The current implementation computes these local distributions using a fixed perplexity (default 30), which has been shown to be a smoother function than fixing the number of neighbors. We address the second issue of interpretation using the inverse Simpson's Index ($1/\sum_{b=1}^{B} p(b)$). The probabilities here refer to the batch probabilities in the local neighborhood distributions described above. This index is the expected number of cells needed to be sampled before two are drawn from the same batch. If the neighborhood consists of only one batch, then only one draw is needed. If it is an equal mix of two batches, two draws are required on average. Thus, this index reports the effective number of batches in a local neighborhood. Our diversity score, LISI, combines these two features: perplexity-based neighborhood construction and the Inverse Simpson's Index. LISI assigns a diversity score to each cell. This score is the effective number of batches in that cell's neighborhood. Code to compute LISI is available as at https://github.com/immunogenomics/LISI. The major shortcoming of LISI is in situations with datasets with vastly different sizes. We demonstrate what happens in this situation in Supplementary Note 2.

Significance between embeddings. In benchmarking against other algorithms, we compared the LISI scores of Harmony to LISI scores of embeddings from other algorithms. We did this with a standard bootstrap estimation framework: first, build an empirical distribution of Harmony LISI values for each cell; then count the frequency with which the observed benchmark LISI is more extreme than bootstrapped LISI values. During the resampling phase, we reran PCA, Harmony and LISI for every bootstrap sample. For P value computation, we used a two-tailed empirical approach, adding 1 to the observed counts to avoid $P = 0$. This calculation is described in the equation below. Let $\widehat{\text{LISI}}_i$ be the observed LISI value for cell i for a benchmarking algorithm. Let LISI_i^b to be LISI value for the bth bootstrap value for cell i. We compute P as

$$P = 2\frac{1 + \min\left(\sum_{b=1}^{B} 1_{\widehat{\text{LISI}}_i > \text{LISI}_i^b}, \sum_{b=1}^{B} 1_{\widehat{\text{LISI}}_i < \text{LISI}_i^b}\right)}{B + 1}$$

Time and memory. We performed execution time and maximum memory usage benchmarks on all analyses. All jobs were run on Linux servers and allotted six cores and 120 GB of memory. The machines were equipped with Intel Xeon E5-2690 v.3 processors. To evaluate execution time and maximal memory usage, we used the Linux time utility (/usr/bin/time on our systems) with the -v flag to record memory usage. Execution time was recorded from the {*Elapsed time*} field. Maximum memory usage was recorded from the {*Maximum resident set size*} field.

Cell-type prediction accuracy. In addition to cLISI, we measured the accuracy of an embedding with cell-type prediction. Briefly, we predict each cell's type based on its neighboring cells and compute accuracy as the frequency of correct predictions. In detail, we compute the 30 nearest neighbors of a cell, based on cosine distance. We then weigh them with an radial basis function kernel with $\sigma = 0.1$ width. Finally, we take the weighted sum over the neighbor's cell types and return the most likely cell type. Formally, for cell i, its 30 nearest cells nearest-neighbor $(NN)(i)$, an embedding matrix Z and cell-type labels vector T, compute the most probable cell-type label t:

$$T_i = \underset{t}{\text{argmax}} \sum_{j \in NN(i)} \exp\left(-\frac{\left\|Z_i/\|Z_i\| - Z_j/\|Zj\|\right\|^2}{\sigma}\right) \times 1_{T_j = t} \qquad (15)$$

Gene expression prediction. We predicted gene expression in the 10X + MERFISH analysis using a similar approach to cell-type prediction above. Instead of predicting cell-type labels T, we predicted gene expression y_g. We predict the expression y_{gi} will take a weighted average of the observed normalized gene expression values of the cell is nearest neighbors.

$$y_{gi} = \underset{t}{\text{argmax}} \sum_{j \in NN(i)} \exp\left(-\frac{\left\|Z_i/Z_i - Z_j/\|Z_j\|\right\|^2}{\sigma}\right) \times y_{gj} \qquad (16)$$

Five-fold cross-validation. In the 10X + MERFISH analysis, we predicted gene expression of the 154 intersecting measured genes with a five-fold cross-validation framework. In this analysis, we removed a randomly sampled one fifth of the genes from both datasets before normalization. We then performed normalization, scaling, PCA and Harmony integration from the remaining four fifths of the genes and predicted the expression of the original removed genes. We repeated this procedure for each of the five holdout genesets. We then repeated the entire procedure ten times, selecting a new random partition in each iteration. We considered the mean of these ten iterations as the predicted value of the gene. We calculated the Pearson correlation between the predicted and measured expression of each gene.

Neuronal subtype correlation. To calculate the correlations between the 10X predicted clusters and the MERFISH clusters, we first subsetted the predicted gene expression matrix to the 154 intersecting 10X/MERFISH genes; we then concatenated the predicted 10X neuronal subtypes to the predicted gene expression matrix and the known neuronal subtypes to the MERFISH dataset. In both the predicted gene expression matrix and the MERFISH dataset, we calculated the average expression of the predicted 10X neuronal subtypes and known neuronal subtypes, respectively. Finally, we calculated the Spearman correlation between the average expression of each predicted 10X inhibitory/excitatory subtype and known MERFISH inhibitory/excitatory subtypes.

Analysis details. *Preprocessing scRNAseq data.* We downloaded raw read or unique molecular identifier matrices for all datasets, from their respective sources. The one exception was the 3pV1 dataset from the PBMC analysis. These data were originally quantified with the hg19 reference, while the other two PBMC datasets were quantified with GRCh38. Thus, we downloaded the fastq files from the 10X website (Supplementary Table 8). We quantified gene expression counts using Cell Ranger[11,41] v.2.1.0 with GRCh38. From the raw count matrices, we used a standard data normalization procedure, laid out below, for all analyses, unless otherwise specified. Except for the $\log_2$ normalization and within-batch variable gene detection, this procedure follows the standard guidelines of the Seurat single-cell analysis platform.

We filtered cells with fewer than 500 genes or more than 20% mitochondrial reads. In the pancreas datasets, we filtered cells with the same thresholds used in Butler et al.[7]: 1,750 genes for Cel-Seq, 2500 genes for Cel-Seq2, no filter for Fluidigm C1, 2500 genes for Smart-Seq2 and 500 genes for inDrop. We then library normalized each cell to 10,000 reads, by multiplicative scaling, then log scaled the normalized data. We then identified the top 1,000 variable genes, ranked by coefficient of variation, within in each dataset. We pooled these genes to form the variable gene set of the analysis. Using only the variable genes, we mean centered and variance 1 scaled the genes across the cells. Note that this was done in the aggregate matrix, with all cells, rather than within each dataset separately. With these values, we performed truncated singular value decomposition keeping the top 30 eigenvectors. Finally, we multiplied the cell embeddings by the eigenvalues to avoid giving eigenvectors equal variance.

Spatial analysis. The raw count 10X and MERFISH datasets were downloaded from their Gene Expression Omnibus and Dryad repositories, respectively. MERFISH metadata was downloaded as a supplementary table from the Moffitt et al. publication[27]. Figures were generated using the six mice from the 10X dataset and the first naive female mouse in the MERFISH dataset. For purposes of prediction all cells labeled as 'Ambiguous' or 'Unstable' were removed from both datasets, as these represent cells with a low number of unique genes expressed, a low library size or a nondeterministic clustering. All genes in the 10X dataset that were not expressed in any cells were removed. In the MERFISH dataset, the gene blanks were removed for integration and the *Fos* gene was removed (no numerical values).

In the 10X dataset, we normalized the counts by dividing the raw counts within each cell by the total number of transcripts within that cell, scaling these counts by 10,000, offsetting the counts by 1 and log transforming the counts. As the MERFISH dataset counts were already normalized by volume, we only performed log transformation on the counts with an offset of 1. We then combined the two datasets by subsetting the 10X dataset to the 154 intersecting genes, concatenating the normalized count matrices and scaling each gene through z-score transformation.

Visualization. We used the UMAP algorithm[42,43] to visualize cells in a two-dimensional space. For all analyses, UMAP was run with the following parameters: $k = 30$ nearest neighbors, correlation based distance and min_dist = 0.1.

Comparison to other algorithms. We used the provided packages or source code provided by the four comparison algorithm publications.

MNN Correct. We used the mnnCorrect function, with default parameters, in the scran R package[44], v.1.9.4. As input, we provided a matrix of PCA embeddings.

Seurat multiCCA. We followed the suggested integration pipeline in the Seurat R package[7], v.2.3.4. This included the RunMultiCCA, MetageneBicorPlot, CalcVarExpRatio, SubsetData (subset.name = 'var.ratio.pca', accept.low = 0.5) and AlignSubspace functions. Unless specified, we used all default parameters for these functions. We used the same number of canonical components as the number of PCs used as input to Harmony, MNN Correct and Scanorama. Unlike the integration examples, we did not scale data within datasets separately, unless otherwise specified. We scaled data on the pooled count matrix instead.

Scanorama. We used the assemble function, with precomputed PCs, from the primary github repository (brianhie/scanorama). We set knn = 30 and sigma = 1, to match the default comparable MNN Correct parameters. All other parameters were kept at default values. We did not use the correct function, as this included both preprocessing and integration of the data. For more equitable comparisons, we tried to use the same preprocessing pipelines for all methods and only compared only the integration steps.

BBKNN. We downloaded the BBKNN software from the primary github repository (Teichlab/bbknn) and followed the suggested integration pipelines, using the bbknn and scanpy umap functions. For the bbknn function, we used $k = 5$ and trim = 20 for all analyses except for the HCA datasets, in which we used $k = 10$ and trim = 30, to accommodate the larger number of cells. All other parameters were kept at default values. Because BBKNN by design constructs a batch-balanced neighborhood graph, LISI should be biased toward these neighbors. On the other hand, BBKNN does not learn a low-dimensional embedding aside from UMAP. Therefore, we were forced to use the potentially biased neighborhood graph provided by the method. We felt that this was appropriate because one step of BBKNN is to prune this graph before the UMAP step. Thus, we used the pruned BBKNN graph to compute LISI.

Harmony parameters. By default, we set the following parameters for Harmony: $\theta = 2$, $K = 100$, $\tau = 0$, $\sigma = 0.1$, block_size = 0.05, $\epsilon_{cluster} = 10^{-5}$, $\epsilon_{harmony} = 10^{-4}$, max_iter$_{cluster}$ = 200, max_iter$_{Harmony}$ = 10, $\lambda =$:1. For the pancreas analysis, we set $\tau = 5$. We set donors to be the primary covariate ($\theta = 2$) and technology secondary ($\theta = 4$). In the spatial analysis, we used $\theta = 3$ and $\lambda = 0.05$.

Identification of alpha and beta ER stress subpopulations. We identified the alpha and beta ER stress clusters in Fig. 5 by performing downstream analysis, specified in this section, on the integrated joint embedding produced by Harmony. After Harmony integration, we performed clustering analysis to find new subtypes. Clustering was done on the trimmed shared nearest-neighbor graph with the Louvain algorithm[45], as implemented in the Seurat package BuildSNN and RunModularityClustering functions. We used the parameters resolution = 0.8, $k = 30$ and nn.eps = 0. We identified several clusters within the alpha, beta and ductal cell populations. For each cluster, we performed differential expression analysis within the defined cell type. That is, we compared alpha clusters to all other alpha cells. For differential expression, we used the R Limma package[18] on the normalized data. We included technology and library complexity (log number of unique genes) as covariates in the linear models. We used the top 100 over-expressed genes for each cluster, weighted by the t-statistic, to perform pathway enrichment with the enrichR[46,47] R package, using the three Gene Ontology genesets[48,49]. The ductal subpopulation was enriched for ribosomal genes; we did not follow up on this cluster.

Labeling cells with canonical markers. In the cell-line, PBMC and pancreas analyses, we labeled cells within individual datasets using canonical markers. We did this by using the standard preprocessing pipeline for each dataset, clustering (Louvain, as above) and identifying clusters specific for the canonical markers for that analysis. We used a similar strategy to identify fine-grained subpopulations of PBMCs and in the HCA 500,000 cell dataset. In these cases, we clustered in the joint embedding produced by Harmony, then looked for clusters that specifically expressed expected canonical markers.

Identification of spatially autocorrelated transcription factors. To identify which of our predicted genes were transcription factors, we downloaded all known vertebrate transcription factors from JASPAR in MEME format[29]. We used this list of transcription factors as a reference for our predicted genes list. We assessed the degree of spatial localization of each transcription factor using Moran's I statistic. Due to the large number of cells, we found the calculation of a dense weights matrix of all pairwise distances between cells to be untenable. Therefore, after taking each slice and centering their respective cell's X and Y centroids around 0, we calculated a sparse weights matrix by finding each MERFISH cell's 30 nearest MERFISH neighbors (using centered X centroids, centered Y centroids and slice Z position as locations for each cell) excluding itself and applying a radial basis

function kernel on the distances of each MERFISH cell's nearest neighbors with bandwidth $\sigma = 60$. For each set of nearest neighbors, we divided each distance by the sum of the distances to obtain probabilities to use as weights, and input these weights into a sparse matrix. Calculations then proceeded as normal from the equation, using the sparse distance matrix as the weights matrix. Genes with significant spatial autocorrelation were evaluated at FDR 0.05. Formally, for gene g, a nearest-neighbor map NN and a three-dimensional spatial embedding matrix X, the nearest-neighbor formulation of Moran's I is

$$I = \frac{N}{\sum_{i,j} w_{ij}} \frac{\sum_{i=1}^{N} \sum_{j \in NN(i)} w_{ij} (y_{gi} - y_g)(y_{gj} - y_g)}{\sum_{i=1}^{N} (y_{gi} - y_g)^2} \qquad (17)$$

$$w_{ij} = \exp\left(-\frac{||X_i - X_j||^2}{\sigma}\right) \qquad (18)$$

ISH Allen Brain Atlas access. To look at the coarse ISH data from Allen Brain Atlas, we used the ISH data portal[31]. We searched for our gene of interest (*Satb1*) and selected experiment number 79488931, with coronal slices. To estimate the anterior-posterior position of each slice, we used the online tool to map each slice to an Atlas reference slice. Each reference slice has a position from the Bregma, searchable in their online Allen Mouse Brain volumetric Atlas: https://scalablebrainatlas.incf.org/mouse/ABA12. The representative image in Fig. 6a is slice 62 (282) in the volumetric atlas. We also used the Atlas annotations online to estimate the location of anatomical structures (that is, hypothalamus and ventricles) in each slice. We downloaded 13 to 16 from experiment 79488931 and focused on a $2 \times 2 \, cm^2$ region around the hypothalamus.

Statistics. Statistical analysis of LISI score comparisons is described in Significance between embeddings. Differential expression tests in the pancreatic islet cell analysis were performed with two-tailed moderated t-tests, implemented in the LIMMA R package. Correlation analyses in the pancreatic islet cell and MERFISH analyses were performed using the Spearman correlation.

Reporting Summary. Further information on research design is available in the Nature Research Reporting Summary linked to this article.

Data availability

All data analyzed in this article are publicly available through online sources. We included links to all data sources in Supplementary Table 8.

Code availability

Harmony and LISI are available as R packages on https://github.com/immunogenomics/harmony and https://github.com/immunogenomics/lisi. Scripts to reproduce results of the primary analyses will be made available on https://github.com/immunogenomics/harmony2019. Additionally, vignettes are included as Supplementary Notes. Supplementary Note 1 provides a detailed walkthrough of Harmony, connecting theoretical algorithm components to their code implementations. Supplementary Note 2 demonstrates the LISI metric and how to evaluate its statistical significance. Supplementary Note 1 uses Harmony with simulated datasets.

References

36. Mao, Q., Wang, L., Goodison, S. & Sun, Y. Dimensionality reduction via graph structure learning. In *Proc. 21th ACM SIGKDD International Conference on Knowledge Discovery and Data Mining*, KDD 2015, 765–774 (ACM, 2015).
37. Dhillon, I. S. & Modha, D. S. Concept decompositions for large sparse text data using clustering. *Mach. Learn.* **42**, 143–175 (2001).
38. Jordan, M. I. & Jacobs, R. A. Hierarchical mixtures of experts and the EM algorithm. *Neural Comput.* **6**, 181–214 (1994).
39. Buttner, M., Miao, Z., Wolf, F. A., Teichmann, S. A. & Theis, F. J. A test metric for assessing single-cell RNA-seq batch correction. *Nat. Methods* **16**, 43–49 (2019).
40. Azizi, E. et al. Single-cell map of diverse immune phenotypes in the breast tumor microenvironment. *Cell* **174**, 1293–1308 (2018).
41. Dobin, A. et al. STAR: ultrafast universal RNA-seq aligner. *Bioinformatics* **29**, 15–21 (2013).
42. McInnes, L. & Healy, J. UMAP: uniform manifold approximation and projection for dimension reduction. Preprint at https://arxiv.org/abs/1802.03426 (2018).
43. Becht, E. et al. Dimensionality reduction for visualizing single-cell data using UMAP. *Nat. Biotechnol.* **37**, 38–44 (2019).
44. Lun, A. T. L., McCarthy, D. J. & Marioni, J. C. A step-by-step workflow for low-level analysis of single-cell RNA-seq data with bioconductor. *F1000 Res.* **5**, 2122 (2016).

45. Blondel, V. D., Guillaume, J.-L., Lambiotte, R. & Lefebvre, E. Fast unfolding of communities in large networks. *J. Stat. Mech.: Theory Exp.* **2008**, P10008 (2008).
46. Chen, E. Y. et al. Enrichr: interactive and collaborative HTML5 gene list enrichment analysis tool. *BMC Bioinformatics* **14**, 128 (2013).
47. Kuleshov, M. V. et al. Enrichr: a comprehensive gene set enrichment analysis web server 2016 update. *Nucleic Acids Res.* **44**, W90–W97 (2016).
48. The Gene Ontology Consortium. Expansion of the gene ontology knowledgebase and resources. *Nucleic Acids Res.* **45**, D331–D338 (2017).
49. Ashburner, M. et al. Gene ontology: tool for the unification of biology. the gene ontology consortium. *Nat. Genet.* **25**, 25–29 (2000).

Author contributions

S.R. and I.K. conceived the research. I.K. led computational work under the guidance of S.R., assisted by N.M., P.L., J.F. and K.S. All authors participated in interpretation and writing the manuscript.

Competing interests

I.K. does paid bioinformatics consulting through Brilyant LLC.

Additional information

Supplementary information is available for this paper at https://doi.org/10.1038/s41592-019-0619-0.

Correspondence and requests for materials should be addressed to S.R.

Peer review information Nicole Rusk was the primary editor on this article and managed its editorial process and peer review in collaboration with the rest of the editorial team.

Reprints and permissions information is available at www.nature.com/reprints.

Corresponding author(s):	Soumya Raychaudhuri
Last updated by author(s):	Jun 20, 2019

Reporting Summary

Nature Research wishes to improve the reproducibility of the work that we publish. This form provides structure for consistency and transparency in reporting. For further information on Nature Research policies, see Authors & Referees and the Editorial Policy Checklist.

Statistics

For all statistical analyses, confirm that the following items are present in the figure legend, table legend, main text, or Methods section.

n/a	Confirmed	
☐	☒	The exact sample size (*n*) for each experimental group/condition, given as a discrete number and unit of measurement
☐	☒	A statement on whether measurements were taken from distinct samples or whether the same sample was measured repeatedly
☐	☒	The statistical test(s) used AND whether they are one- or two-sided *Only common tests should be described solely by name; describe more complex techniques in the Methods section.*
☐	☒	A description of all covariates tested
☐	☒	A description of any assumptions or corrections, such as tests of normality and adjustment for multiple comparisons
☐	☒	A full description of the statistical parameters including central tendency (e.g. means) or other basic estimates (e.g. regression coefficient) AND variation (e.g. standard deviation) or associated estimates of uncertainty (e.g. confidence intervals)
☐	☒	For null hypothesis testing, the test statistic (e.g. *F*, *t*, *r*) with confidence intervals, effect sizes, degrees of freedom and *P* value noted *Give P values as exact values whenever suitable.*
☒	☐	For Bayesian analysis, information on the choice of priors and Markov chain Monte Carlo settings
☒	☐	For hierarchical and complex designs, identification of the appropriate level for tests and full reporting of outcomes
☐	☒	Estimates of effect sizes (e.g. Cohen's *d*, Pearson's *r*), indicating how they were calculated

Our web collection on statistics for biologists contains articles on many of the points above.

Software and code

Policy information about availability of computer code

Data collection	Synthetic data was generated using custom scripts, available in Supplementary Note 3, attached with this manuscript.
Data analysis	We used custom scripts for preprocessing data. The code for Harmony is deposited on github.com/immunogenomics/harmony. The code for LISI is desposited on github.com/immugenomics/lisi. We used the following open source R packages for various analyses: scran version 1.9.4; Seurat version 2.3.4; limma version 3.40.2; enrichR version 1.0. Open source python scripts were downloaded from github: brianhie/scanorama and Teichlab/bbknn.

For manuscripts utilizing custom algorithms or software that are central to the research but not yet described in published literature, software must be made available to editors/reviewers. We strongly encourage code deposition in a community repository (e.g. GitHub). See the Nature Research guidelines for submitting code & software for further information.

Data

Policy information about availability of data

All manuscripts must include a data availability statement. This statement should provide the following information, where applicable:
- Accession codes, unique identifiers, or web links for publicly available datasets
- A list of figures that have associated raw data
- A description of any restrictions on data availability

All data analyzed in this manuscript are publicly available through online sources. We included links to all data sources in Table S8.

Field-specific reporting

Please select the one below that is the best fit for your research. If you are not sure, read the appropriate sections before making your selection.

☒ Life sciences   ☐ Behavioural & social sciences   ☐ Ecological, evolutionary & environmental sciences

Life sciences study design

All studies must disclose on these points even when the disclosure is negative.

Sample size	We had no statistical tests that required the determination of sample size
Data exclusions	We filtered cells with fewer than 500 genes or more than 20% mitochondrial reads. In the pancreas datasets, we filtered cells with the same thresholds used in Butler et al:7 1750 genes for CelSeq, 2500 genes for CelSeq2, no filter for Fluidigm C1, 2500 genes for SmartSeq2, and 500 genes for inDrop.
Replication	We demonstrate the performance of Harmony on a variety of real and synthetic datasets.
Randomization	N/A
Blinding	N/A

Reporting for specific materials, systems and methods

We require information from authors about some types of materials, experimental systems and methods used in many studies. Here, indicate whether each material, system or method listed is relevant to your study. If you are not sure if a list item applies to your research, read the appropriate section before selecting a response.

Materials & experimental systems

n/a	Involved in the study
☒ ☐	Antibodies
☒ ☐	Eukaryotic cell lines
☒ ☐	Palaeontology
☒ ☐	Animals and other organisms
☒ ☐	Human research participants
☒ ☐	Clinical data

Methods

n/a	Involved in the study
☒ ☐	ChIP-seq
☒ ☐	Flow cytometry
☒ ☐	MRI-based neuroimaging